AIAA SciTech Forum
8-12 January 2024, Orlando, FL
AIAA SCITECH 2024 Forum

10.2514/6.2024-0492

Analysis of CoFlow Wall Jet in Extreme Adverse Pressure Gradient with Super-Lift Coefficient

B. McBreen,[*] E. Butler, [†] G.-C. Zha,[‡]
Dept. of Mechanical and Aerospace Engineering
University of Miami, Coral Gables, Florida 33146
E-mail: gzha@miami.edu

Abstract

This paper presents the findings of a 2D numerical study of flows in Extreme Adverse Pressure Gradients (EAPG) enabled by Co-Flow Jet (CFJ) Active Flow Control (AFC). We define an EAPG to be an adverse pressure gradient that is at least ten times larger than the maximum adverse pressure gradient sustainable by the non-controlled flow of a baseline case at the same conditions. The flow field is solved using a set of 2D one-equation Spalart-Allmaras turbulence model. A CFJ cylinder and CFJ airfoil with EAPG and attached flow are studied at Mach number 0.063, and Reynolds numbers $5.62 \times 10^5 - 1.69 \times 10^6$. The CFJ cylinder achieves time-averaged lift coefficients up to $C_L = 26.718$ with $C_\mu = 10.0$, and the CFJ airfoil shows time-averaged lift coefficients up to $C_L = 13.411$ with $C_\mu = 12.0$. The injection jet remains subsonic for both the cylinder and the airfoil, reducing the power required compared to previous studies, which reach supersonic injection jet speeds. The CFJ cylinder measures a maximum streamwise pressure gradient 14 times the strength of its baseline, while the the CFJ airfoil reports a much higher adverse pressure gradient that is 879 times greater than its baseline counterpart. Such extraordinary lift generation and adverse pressure gradient ratios motivate this effort to investigate how the implementation of the CFJ can achieve this effect. The exceptional lift coefficients presented exceed the classically defined limit for $C_{L_{max}}$, and are termed "Super-Lift Coefficients" (SLCs). Supporting spatial mesh and time step refinement studies, conducted subsequently, show nearly identical results. Evaluating boundary layer flow attachment via the turbulent wall jet momentum equation, this study finds that the turbulent eddy viscosity diffusion near the wall is the most significant factor offsetting the adverse pressure gradient to maintain attached flow. The turbulence diffusion near the wall has a degree of uncertainty due to the use of the S-A RANS turbulence model. To ensure the EAPG phenomenon is captured within RANS models' uncertainty, a CFJ cylinder case with C_L of 22.89 is simulated using the two-equation k-ω SST model, which gives a C_L of 20.365, only differed by 11% and is acceptable for RAND models. Further studies with high fidelity simulation of LES, DNS, and experiment to verify the EAPG phenomenon are desirable.

Nomenclature

$AoA,\ \alpha$	Angle of Attack
APG	Adverse Pressure Gradient
$EAPG$	Extreme Adverse Pressure Gradient
CFJ	Co-Flow Jet
SLC	Super-Lift Coefficient
$PG_x,\ PG_s$	Normalized Streamwise Pressure Gradient, $\frac{C}{0.5\rho_\infty V_\infty^2}\frac{\partial p}{\partial x}$
$PG_y,\ PG_r$	Normalized Radial Pressure Gradient, $\frac{C}{0.5\rho_\infty V_\infty^2}\frac{\partial p}{\partial r}$

---

[*] Ph.D. Candidate

[†] Masters Student

[‡] Professor, AIAA Associate Fellow

PGR_x	Streamwise Pressure Gradient Ratio, $PG_{x\ CFJ}/PG_{x\ Baseline}$
PGR_r	Radial Pressure Gradient Ratio, $PG_{r\ CFJ}/PG_{r\ Baseline}$
P	CFJ pumping power consumption, $P = \frac{\dot{m} C_p T_{t2}}{\eta}(\Gamma^{\frac{\gamma-1}{\gamma}} - 1)$
η	CFJ pumping system efficiency, propeller efficiency
P_c	Power coefficient, $P_c = \frac{P}{\frac{1}{2}\rho_\infty V_\infty^3 S}$
C_μ	Jet momentum coefficient, $C_\mu = \frac{\dot{m} V_j}{\frac{1}{2}\rho_\infty {V_\infty}^2 S}$
C_L	Lift coefficient
C_D	Drag coefficient
$(C_L/C_D)_c$	Aerodynamic efficiency corrected for CFJ airfoil, $\frac{L}{D+P/V_\infty}$
Re	Reynolds number
Ma	Mach number
γ	Air specific heat ratio
ρ_∞	Freestream density
V_∞	Freestream velocity
T_t	Total temperature
P_t	Total pressure
H_t	Total specific enthalpy
$\dot{m}$	Mass flow rate through the CFJ
ω_z	Spanwise Vorticity
C, c	Chord length
r_c	Radius of Curvature
κ	Curvature, $1/r_c$

1 Introduction

Active Flow Control (AFC) is a means by which flow systems may substantially extend their operating limits — delaying stall and increasing lift. An AFC system may overcome adverse pressure gradients within the flow by adding energy into the boundary layer. The Co-Flow Jet (CFJ) active flow control technique has been studied for its ability to drastically increase an airfoil's stall margin [1, 2, 3, 4], aerodynamic efficiency [5, 6, 7, 8, 9], and lift [3, 2, 10, 11]. Previous work by this research group has shown that the CFJ enables super-lift coefficients by sustaining an Extreme Adverse Pressure Gradient (EAPG) and maintaining attached flow [12, 13, 14, 15]. We define an Extreme Adverse Pressure Gradient (EAPG) to be an adverse pressure gradient with a magnitude exceeding ten times the maximum APG that its non-controlled counterpart flow can sustain for the same conditions. This paper builds upon previous work to ask the question "Why can the CFJ sustain such high EAPGs?"

A flow system's $C_{L_{max}}$ is limited by the maximum adverse pressure gradient it can sustain before stalling. Once the critical APG is reached, the flow can no longer adhere to the surface and the system will experience stall. Stall effectively sets the upper limit for the lift coefficient. Understanding and managing APG is crucial for optimizing a flow system's performance, especially in conditions demanding high lift. The airfoil is the most common fluid system limited by the APG and stall. As an airfoil rotates to higher angles of attack, the adverse pressure gradient it can sustain on the suction surface increases until the onset of separated flow. The maximum streamwise pressure gradient occurs on the surface immediately upstream of the separation onset location. Once the flow is separated, the pressure gradient is relaxed in the flow separated region.

Co-Flow Jet AFC is a zero-net-mass-flux flow control using fluidic actuators developed by Zha and his team. The CFJ airfoil has a tangential injection slot near the leading edge (LE) of the airfoil's suction surface and a streamwise suction slot near the trailing edge (TE), shown in Fig. 1. A small amount of the flow is ingested into the airfoil through the suction slot, pressurized and energized by a micro-compressor inside the airfoil, then injected near the leading edge through the injection slot. The CFJ airfoil is known for its high control authority due to its very high stall AoA, ultra-high lift coefficient, and very low energy expenditure. Co-Flow Jet injection is tangent to the airfoil's surface, making it a wall jet. Since jet injection usually causes turbulence transition in the flow, the CFJ's injection jet is categorized as turbulent wall jet [15].

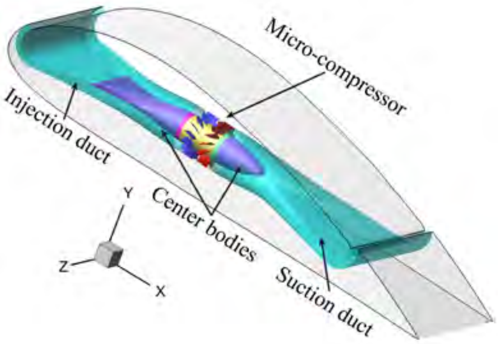

schematic.png

Figure 1: Schematic of components making up CFJ airfoil.

The maximum lift coefficient an airfoil can create is governed by the maximum adverse pressure gradient (APG) that it can sustain before stalling. Smith [16] gives the following maximum lift coefficient limit, based on potential flow theory and the Kutta condition at an angle of attack of 90°:

$$C_{Lmax} = 2\pi(1 + \frac{t}{c}) \tag{1}$$

For a cylinder with $t/c = 1$, the C_{Lmax} limit will be $4\pi = 12.56$ and is consistent with Prandtl's conclusion [17]. However, the cylinder C_{Lmax} limit was exceeded by Lockwood et al. in 1960 [18] using multiple tangential blowing slots on the cylinder surface. They achieved $C_{Lmax} \approx 20$ with an injection momentum coefficient of $C_\mu \approx 5$. Tokumaru and Dimotakis in 1993 [19] achieved $C_{Lmax} \approx 14$ by using a rotating cylinder. Based on potential flow theory, the stagnation point should be detached from the cylinder surface when C_{Lmax} is greater than 4π. A maximum lift coefficient that exceeds the C_{Lmax} defined in Eq. (1) is termed a "Super-Lift Coefficient" (SLC) [3].

Yang and Zha were the first to apply CFJ active flow control to a cylinder [20]. Their simulations used 2D RANS simulation with the one-equation Spalart-Allmaras turbulence model [21]. Their CFJ cylinder achieved a $C_{Lmax} \approx 28$ at $C_\mu = 0.8$, far exceeding $C_{Lmax} = 4\pi$. This super-lift result came at the cost of a very high power coefficient, $P_c \approx 22.5$, and a CFJ total pressure ratio $P_{02}/P_{01} \approx 4.5$. Yang and Zha further applied CFJ AFC to the CFJ-NACA6421 airfoil at a free-stream Mach number of 0.063 [3]. They stated that there appears to be no limit to the C_{Lmax} for a CFJ airfoil, so long as the jet can continue adding energy to the flow. They note that the power required is exponentially proportional to the C_{Lmax}, and observe that the CFJ airfoil's maximum lift capacity is limited by the adverse pressure gradient. The stronger the adverse pressure gradient, the more difficult it is for the injection jet to add energy to the flow. While Yang and Zha identified SLC conditions for their CFJ airfoil and cylinder studies, they did not quantify the EAPG and its contribution to the SLC.

The purpose of this study is to investigate the flow attachment mechanism of the wall jet boundary layer in an EAPG for a CFJ cylinder and airfoil with SLC. The CFJ configurations are redesigned to have substantially lower power coefficients.

The pressure gradient coefficients in the streamwise and centrifugal directions are defined as:

$$PG_x = PG_s = \frac{C}{0.5\rho_\infty V_\infty^2}\frac{\partial p}{\partial s}, \quad PG_r = \frac{C}{0.5\rho_\infty V_\infty^2}\frac{\partial p}{\partial r} \approx \frac{C}{0.5\rho_\infty V_\infty^2}\frac{\rho V_t^2}{R} \tag{2}$$

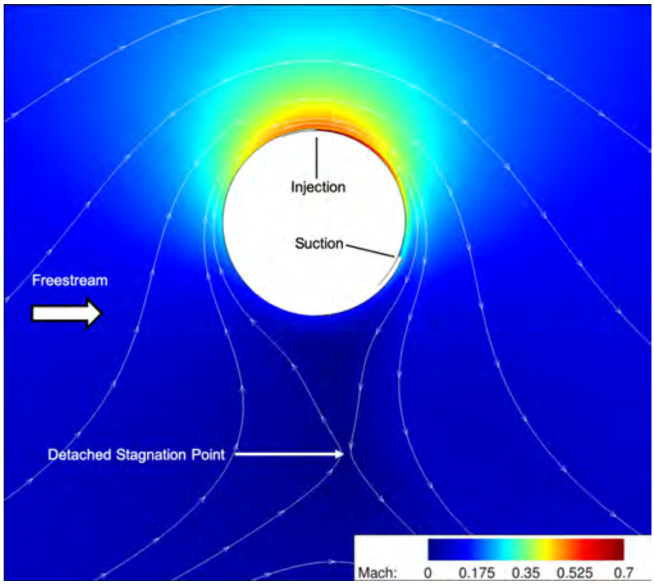

Figure 2: CFJ cylinder steady Mach contours and streamlines at $Ma_\infty = 0.1$ $C_\mu = 0.7$ [12]

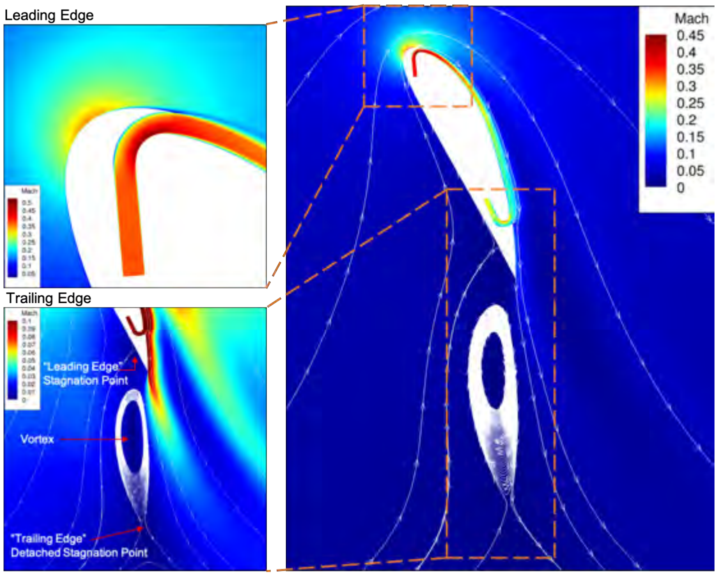

Figure 3: CFJ6421 airfoil steady Mach contours and streamlines at $C_\mu = 4.5$ and AoA = 65° [12]

where the subscript x or s denotes the streamwise direction, and r denotes the radial direction transverse to the flow. C is the airfoil chord, V_t is the streamwise velocity, which is tangent to the local surface, and R is the local curvature radius. When these adverse pressure gradients exceed ten times the maximum APG that the non-controlled counterpart flow can sustain, we refer to them as Extreme Adverse Pressure Gradient (EAPGs). Thus for comparison purposes, the streamwise and radial pressure gradient ratios are:

$$PGR_x = PGR_s = \frac{PG_{s\ CFJ}}{PG_{s\ Baseline}}, \quad PGR_r = \frac{PG_{r\ CFJ}}{PG_{r\ Baseline}} \tag{3}$$

Fig. 2 shows example Mach contours with streamlines for a steady-state simulation of the CFJ cylinder at Ma=0.1 and $C_\mu = 0.7$, which has a $C_L = 18.20$ [12]. The CFJ completely removes the flow separation caused by vortex shedding behind the cylinder. The stagnation point is detached from the solid surface, in line with predictions from potential flow theory ($18.20 > 4\pi$). Fig. 3 shows that the studied CFJ-NACA6421 airfoil had attached flow at AoA of 65° and $C_\mu = 4.5$ with a $C_L = 15.96$, which exceeds the potential flow limit of 7.6. The circulation is so high that the stagnation point detaches from the airfoil sharp trailing edge. The trailing edge vortex creates a circulation and lifting effect approximately equivalent to an extension of the airfoil solid body to the stagnation point. The stagnation point detachment from a sharp airfoil trailing edge had not appeared to be documented in fluid mechanics literature until the observation of Yang and Zha [3] in 2017 and seems to contradict the Kutta condition. Yang and Zha [3] argue that it does not violate flow physics, remarking that the Kutta condition is a mathematical condition to enforce a unique solution of potential flows. It is not a physical condition that real flows or Navier-Stokes equations must satisfy. When the circulation exceeds the limit, the trailing edge stagnation point can detach in the same manner as the spinning cylinder, and the lift coefficient will continue to increase with increased circulation.

This paper numerically examines the flows with an EAPG enabled by the CFJ. Xu et al [15] have analyzed the CFJ separation control mechanism in an APG using the NASA hump case [22]. The APG of the NASA hump is mild, and is not an EAPG.

1.1 Evaluating Flow Attachment with the Turbulent Wall Jet Momentum Equation

The 2D turbulent wall jet momentum equation is used to evaluate the flow attachment on the surface. Derived from the fluid momentum equation for turbulent wall jets [15], Eq. (4) assumes that the local wall curvature is small and that body force is neglected. In the below equations, x refers to the local streamwise direction tangent to the wall surface, and y is the normal direction to the wall surface. The turbulent wall jet momentum equation in x direction can be written as the following, in partial difference form [15]:

$$\rho u\frac{\partial u}{\partial x}+\rho v\frac{\partial u}{\partial y}-\frac{1}{Re}\frac{\partial \mu}{\partial y}\frac{\partial u}{\partial y}+\frac{\partial p}{\partial x}=\frac{1}{Re}\mu\frac{\partial^2 u}{\partial y^2} \tag{4}$$

The viscosity μ is composed of the molecular viscosity and turbulent eddy viscosity. The derivation of the wall jet momentum equation in cylindrical coordinates (not shown) to include the curvature effect results in a similar form to Eq. (4). Thus Eq. (4) can be used to guide the wall jet analysis with high curvature configuration.

Schlichiting and Gersten [23] give the compatibility condition at the wall as the following. This expression is a general condition for 2D flows regardless of whether the flow is laminar or turbulent, separated or attached.

$$\left.\frac{\partial p}{\partial x}\right|_{y=0}=\mu\left.\frac{\partial^2 u}{\partial y^2}\right|_{y=0} \tag{5}$$

Eq. (5) is obtained from the 2D Navier–Stokes equations with a no-slip wall condition and assumes a zero molecular viscosity gradient within the viscous sub-layer. This expression shows that the sign of $\partial^2 u/\partial y^2$ at the wall is determined by the sign of the pressure gradient. Flow with a favorable pressure gradient is attached with the flow condition at the wall $[\partial^2 u/\partial y^2]_w < 0$, and the velocity profile has no inflection point. For flow in an adverse pressure gradient ($\partial p/\partial x > 0$), the sign of $\partial^2 u/\partial y^2$ is also positive. A more general criterion for separation control is suggested by Xu et al. [15]. The attached velocity profiles will have $\tau_w > 0 \ \ (\partial u/\partial y > 0,\ \omega_z < 0)$ with $[\partial^2 u/\partial y^2]_w \geq 0$. The $[\partial^2 u/\partial y^2]_w = 0$ case includes zero pressure gradient situations. If $\partial u/\partial y < 0$, the flow is separated [15].

An APG *can* be overcome along a wall when considering the effects of flow convection and diffusion. The first two terms on the LHS of Eq. (4) are the convective terms, which are responsible for transferring the wall jet momentum in the streamwise and transverse flow directions. In the wall jet, these two terms are similar in magnitude due to the high velocity gradient imposed by the CFJ injection[15]. The third term is the turbulent diffusion due to the turbulent eddy viscosity gradient. This term is negligible for laminar flow since the viscosity is fairly constant, but is dominant for the turbulent wall jet mixing due to the rapid growth rate of turbulent eddy viscosity near the wall. This turbulent diffusion is of particular interest in addressing the postulation of this paper. The effect of the turbulent diffusion will be discussed in more detail in Section **??**. All of the first three terms on the LHS of Eq. 4 are responsible for offsetting the adverse pressure gradient, however the diffusion term plays the most significant role in transferring momentum inward to energize the boundary layer, and outward to entrain the main flow.

Eq. (4) can be expressed in terms of spanwise vorticity, with the substitution:

$$\omega_z=\frac{\partial v}{\partial x}-\frac{\partial u}{\partial y}\approx-\frac{\partial u}{\partial y} \tag{6}$$

A wall jet's injection flow tangent to the wall surface has $\frac{\partial v}{\partial x} << \frac{\partial u}{\partial y}$ except in the region close to the suction slot entrance. The wall jet momentum Eq. 4 may then be rewritten as:

$$\rho u\frac{\partial u}{\partial x} - \rho v\omega_z + \frac{\omega_z}{Re}\frac{\partial \mu}{\partial y} + \frac{\partial p}{\partial x} = \frac{\mu}{Re}\frac{\partial^2 u}{\partial y^2} \tag{7}$$

The strong spanwise vorticity flux along the walls of the injection duct play a crucial role in attaching the injection jet flow in the presence of an EAPG.

2 Numerical Algorithms

The Improved Delayed Detached Eddy Simulation (IDDES) solver implemented and validated by Yang and Zha [4, 11] is adopted in this study, applied in two dimensions. Since IDDES is a hybrid model of RANS near the wall and Large Eddy Simulation (LES) away from the wall, the simulation must be three-dimensional to resolve the large eddies. The 2D application of this model represents predominantly the URANS model. However, the 2D IDDES model is more robust numerically.

2.1 Governing Equations

The spatially filtered Navier-Stokes governing equations in generalized coordinates are expressed as:

$$\tfrac{\partial \mathbf{Q}}{\partial t} + \tfrac{\partial \mathbf{E}}{\partial \xi} + \tfrac{\partial \mathbf{F}}{\partial \eta} + \tfrac{\partial \mathbf{G}}{\partial \zeta} = \tfrac{1}{Re}\left(\tfrac{\partial \mathbf{E}_v}{\partial \xi} + \tfrac{\partial \mathbf{F}_v}{\partial \eta} + \tfrac{\partial \mathbf{G}_v}{\partial \zeta} + \mathbf{S}\right) \tag{8}$$

where Re is the Reynolds number. The equations are normalized based on airfoil chord L_∞, freestream density ρ_∞ and velocity U_∞.

The conservative variable vector $\mathbf{Q}$, the inviscid flux vectors $\mathbf{E}$, $\mathbf{F}$, $\mathbf{G}$, the viscous flux $\mathbf{E_v}$, $\mathbf{F_v}$, $\mathbf{G_v}$ and the source term vector $\mathbf{S}$ are expressed as

$$\mathbf{Q} = \frac{1}{J}\begin{pmatrix} \bar{\rho} \\ \bar{\rho}\tilde{u} \\ \bar{\rho}\tilde{v} \\ \bar{\rho}\tilde{w} \\ \bar{\rho}\tilde{e} \\ \bar{\rho}\tilde{\nu}_t \end{pmatrix}, \mathbf{E} = \begin{pmatrix} \bar{\rho}U \\ \bar{\rho}\tilde{u}U + l_x\bar{p} \\ \bar{\rho}\tilde{v}U + l_y\bar{p} \\ \bar{\rho}\tilde{w}U + l_z\bar{p} \\ \left(\bar{\rho}\tilde{e} + \bar{p}\right)U - l_t\bar{p} \\ \bar{\rho}\tilde{\nu}U \end{pmatrix}, \mathbf{F} = \begin{pmatrix} \bar{\rho}V \\ \bar{\rho}\tilde{u}V + m_x\bar{p} \\ \bar{\rho}\tilde{v}V + m_y\bar{p} \\ \bar{\rho}\tilde{w}V + m_z\bar{p} \\ \left(\bar{\rho}\tilde{e} + \bar{p}\right)V - m_t\bar{p} \\ \bar{\rho}\tilde{\nu}V \end{pmatrix}, \mathbf{G} = \begin{pmatrix} \bar{\rho}W \\ \bar{\rho}\tilde{u}W + n_x\bar{p} \\ \bar{\rho}\tilde{v}W + n_y\bar{p} \\ \bar{\rho}\tilde{w}W + n_z\bar{p} \\ \left(\bar{\rho}\tilde{e} + \bar{p}\right)W - n_t\bar{p} \\ \bar{\rho}\tilde{\nu}W \end{pmatrix} \tag{9}$$

$$\mathbf{E_v} = \begin{pmatrix} 0 \\ l_k\bar{\tau}_{xk} \\ l_k\bar{\tau}_{yk} \\ l_k\bar{\tau}_{zk} \\ l_k\left(\tilde{u}_i\bar{\tau}_{ki} - \bar{q}_k\right) \\ \frac{\bar{\rho}}{\sigma}\left(\nu + \tilde{\nu}\right)\left(\mathbf{l} \bullet \nabla\tilde{\nu}\right) \end{pmatrix}, \mathbf{F_v} = \begin{pmatrix} 0 \\ m_k\bar{\tau}u_{xk} \\ m_k\bar{\tau}_{yk} \\ m_k\bar{\tau}u_{zk} \\ m_k\left(\tilde{u}_i\bar{\tau}_{ki} - \bar{q}_k\right) \\ \frac{\bar{\rho}}{\sigma}\left(\nu + \tilde{\nu}\right)\left(\mathbf{m} \bullet \nabla\tilde{\nu}\right) \end{pmatrix}, \mathbf{G_v} = \begin{pmatrix} 0 \\ n_k\bar{\tau}_{xk} \\ n_k\bar{\tau}_{yk} \\ n_k\bar{\tau}_{zk} \\ n_k\left(\tilde{u}_i\bar{\tau}_{ki} - \bar{q}_k\right) \\ \frac{\bar{\rho}}{\sigma}\left(\nu + \tilde{\nu}\right)\left(\mathbf{n} \bullet \nabla\tilde{\nu}\right) \end{pmatrix} \tag{10}$$

$$\mathbf{S} = \frac{1}{J}\begin{pmatrix} 0 \\ 0 \\ 0 \\ 0 \\ 0 \\ 0 \\ S_\nu \end{pmatrix} \tag{11}$$

where ρ is the density, p is the static pressure, and e is the total energy per unit mass. The overbar term denotes a regular filtered variable in the LES region,or a Reynolds-averaged value in the RANS region. And the tilde symbol is used to denote the Favre filtered variable. ν is kinematic viscosity and $\tilde{\nu}$ is the working variable related to eddy viscosity in S-A and IDDES turbulence one equation model [21]. U, V and W are the contravariant velocities in ξ, η, ζ directions, and defined as

$$\begin{aligned} U &= l_t + \mathbf{l} \bullet \mathbf{V} = l_t + l_x\tilde{u} + l_y\tilde{v} + l_z\tilde{w} \\ V &= m_t + \mathbf{m} \bullet \mathbf{V} = m_t + m_x\tilde{u} + m_y\tilde{v} + m_z\tilde{w} \\ W &= n_t + \mathbf{n} \bullet \mathbf{V} = n_t + n_x\tilde{u} + n_y\tilde{v} + n_z\tilde{w} \end{aligned} \tag{12}$$

where J is the Jacobian of the coordinate transformation. l_t, m_t and n_t are the components of the interface contravariant velocity of the grid in ξ, η and ζ directions respectively. $\mathbf{l}$, $\mathbf{m}$ and $\mathbf{n}$ denote the normal vectors located at the centers of ξ, η and ζ interfaces of the control volume with their magnitudes equal to the surface areas and pointing to the directions of increasing ξ, η and ζ.

$$\mathbf{l} = \frac{\nabla\xi}{J},\ \mathbf{m} = \frac{\nabla\eta}{J},\ \mathbf{n} = \frac{\nabla\zeta}{J} \tag{13}$$

$$l_t = \frac{\xi_t}{J},\ m_t = \frac{\eta_t}{J},\ n_t = \frac{\zeta_t}{J} \tag{14}$$

In the generalized coordinates, $\Delta\xi = \Delta\eta = \Delta\zeta = 1$. Since the DES-family approach is based on S-A model, the formulations of the original S-A model are given below. The source term S_ν from the S-A model in Eq. 11 is given by

$$\begin{aligned} S_\nu = \bar{\rho}C_{b1}\left(1 - f_{t2}\right)\tilde{S}\tilde{\nu} + \tfrac{1}{Re}\Big[-\bar{\rho}\left(C_{w1}f_w - \tfrac{C_{b1}}{\kappa^2}f_{t2}\right)\left(\tfrac{\tilde{\nu}}{d}\right)^2 \\ + \tfrac{\bar{\rho}}{\sigma}C_{b2}\left(\nabla\tilde{\nu}\right)^2 - \tfrac{1}{\sigma}\left(\nu + \tilde{\nu}\right)\nabla\tilde{\nu} \bullet \nabla\bar{\rho}\Big] + Re\left[\bar{\rho}f_{t1}\left(\Delta q\right)^2\right] \end{aligned} \tag{15}$$

where

$$\chi = \frac{\tilde{\nu}}{\nu}, \qquad f_{v1} = \frac{\chi^3}{\chi^3 + c_{v1}^3}, \qquad f_{v2} = 1 - \frac{\chi}{1 + \chi f_{v1}}, \qquad f_{t1} = C_{t1}g_t exp\left[-C_{t2}\frac{\omega_t^2}{\Delta U^2}\left(d^2 + g_t^2 d_t^2\right)\right] \tag{16}$$

$$f_{t2} = C_{t3}exp\left(-C_{t4}\chi^2\right), \qquad f_w = g\left(\frac{1 + c_{w3}^6}{g^6 + c_{w3}^6}\right)^{1/6}, \qquad g = r + c_{w2}(r^6 - r) \tag{17}$$

$$g_t = min\left(0.1, \frac{\Delta q}{\omega_t \Delta x_t}\right), \qquad \tilde{S} = S + \frac{\tilde{\nu}}{k^2 d^2 R_e}f_{v2}, \qquad r = \frac{\tilde{\nu}}{\tilde{S}k^2 d^2 R_e} \tag{18}$$

where ω_t is the wall vorticity at the wall boundary layer trip location, d is the distance to the closest wall, d_t is the distance of the field point to the trip location, Δq is the difference of the velocities between the field point and the trip location, Δx_t is the grid spacing along the wall at the trip location. The values of the coefficients are: $c_{b1} = 0.1355, c_{b2} = 0.622, \sigma = \frac{2}{3}, c_{w1} = \frac{c_{b1}}{k^2} + (1 + c_{b2})/\sigma, c_{w2} = 0.3, c_{w3} = 2, k = 0.41, c_{v1} = 7.1, c_{t1} = 1.0, c_{t2} = 2.0, c_{t3} = 1.1, c_{t4} = 2.0$. The details of the IDDES formulations can be seen in Yang and Zha [4, 11].

2.2 Time Marching Scheme

Following the dual time stepping method suggested by Jameson [24], an implicit pseudo time marching scheme using line Gauss-Seidel line relaxation is employed to solve the governing equations, as the following:

$$\frac{\partial \mathbf{Q}}{\partial t} = \frac{\mathbf{3Q^{n+1} - 4Q^{n} + Q^{n-1}}}{2\Delta t} \tag{19}$$

where $n-1$, n and $n+1$ are three sequential time levels, which have a time interval of Δt. The first-order Euler scheme is used to discretize the pseudo temporal term. The semi-discretized equations of the governing equations are given as the following:

$$\begin{aligned} &\left[\left(\tfrac{1}{\Delta \widehat{\tau}} + \tfrac{1.5}{\Delta t}\right) I - \left(\tfrac{\partial R}{\partial \mathbf{Q}}\right)^{n+1,m}\right] \delta \mathbf{Q}^{\mathbf{n+1,m+1}} \\ &= R^{n+1,m} - \tfrac{\mathbf{3Q^{n+1,m} - 4Q^{n} + Q^{n-1}}}{2\Delta t} \end{aligned} \tag{20}$$

where the $\Delta \widehat{\tau}$ is the pseudo time step, and R stands for the net flux determined by the spatial high order numerical scheme, m is the iteration index for the pseudo time. A non-dimensional physical time-step of 0.005 is used for the present study.

2.3 Navier-Stokes Solver

The in-house high order accuracy CFD code Flow-Acoustics-Structure Interaction Package (FASIP) is used to conduct the IDDES. The 3D Navier-Stokes equations are solved by a 5th order WENO scheme for the inviscid fluxes [25, 26, 27] and a 4th order central differencing scheme for the viscous terms [26]. The low diffusion E-CUSP scheme suggested by Zha et al [28] is used as the approximate Riemann solver. This scheme is based on the Zha-Bilgen flux-vector-splitting scheme [29] and is utilized with the WENO scheme to evaluate the inviscid fluxes. An implicit unfactored time marching method using Gauss-Seidel line relaxation is used to achieve a fast convergence rate [30]. Parallel computing is implemented to save simulation time [31]. The FASIP code has been intensively validated for CFJ flow control simulations [32, 33, 34, 35, 36, 37, 38, 13, 39].

2.4 Co-Flow Jet Parameters

2.4.1 Lift and Drag Calculation

The momentum and pressure at the injection and suction slots produce a reactionary force not included in the surface integral used to calculate lift and drag on the airfoil surface. Using control volume analysis, the reactionary force can be calculated using the flow parameters at the injection and suction slot opening surfaces. Zha et al. [38] give the following formulations to calculate the lift and drag due to the jet reactionary force for a CFD simulation.

By considering the effects of injection and suction jets on the CFJ airfoil, the expressions for these reactionary forces are given as:

$$F_{x_{cfj}} = (\dot{m}_j V_{j1} + p_{j1} A_{j1}) * \cos(\theta_1 - \alpha) - (\dot{m}_j V_{j2} + p_{j2} A_{j2}) * \cos(\theta_2 + \alpha) \tag{21}$$

$$F_{y_{cfj}} = (\dot{m}_{j1} V_{j1} + p_{j1} A_{j1}) * \sin(\theta_1 - \alpha) + (\dot{m}_{j2} V_{j2} + p_{j2} A_{j2}) * \sin(\theta_2 + \alpha) \tag{22}$$

where the subscripts 1 and 2 stand for the injection and suction respectively, and θ_1 and θ_2 are the angles between the injection and suction slot surfaces and a line normal to the airfoil chord. α is the angle of attack.

The total lift and drag on the airfoil can then be expressed as:

$$D = R'_x - F_{x_{cfj}} \tag{23}$$

$$L = R'_y - F_{y_{cfj}} \tag{24}$$

where R'_x and R'_y are the surface integral of pressure and shear stress in x (drag) and y (lift) direction excluding the internal ducts of injection and suction, and $F_{x_{cfj}}$ and $F_{y_{cfj}}$ are the CFJ jet reaction forces. For the CFD simulation, the total lift and drag are calculated using Eqns. 23 and 24.

2.4.2 CFJ Aerodynamic Efficiency

The conventional airfoil aerodynamic efficiency is defined as $\frac{L}{D}$. However since CFJ active flow control consumes energy, the CFJ corrected aerodynamic efficiency is modified to take into account the energy consumption of the pump. The formulation of the corrected aerodynamic efficiency for CFJ airfoils is :

$$\left(\frac{C_L}{C_D}\right)_c = \frac{L}{D + \frac{P}{V_\infty}} = \frac{C_L}{C_D + P_C} \tag{25}$$

where V_∞ is the freestream velocity, P is the CFJ pumping power, and L and D are the lift and drag generated by the CFJ airfoil. This formulation converts the power consumed by the CFJ into the drag of the airfoil.

2.4.3 CFJ Power Coefficient

The CFJ can be implemented via a pumping system inside the wing that withdraws air from the suction slot and blows it into the injection slot. As a Zero-Net-Mass-Flux (ZNMF) flow control mechanism with a closed flow path, the CFJ power required can be defined by thermodynamic relationship between the mass flow rate and total enthalpy variation. The power consumption can be determined by the jet mass flow and total enthalpy change as the following:

$$P = \dot{m}(H_{t1} - H_{t2}) \tag{26}$$

where H_{t1} and H_{t2} are the total enthalpy in the injection cavity and suction cavity respectively, P is the power required by the pump and $\dot{m}$ the jet mass flow rate. Introducing the pumping efficiency η and total pressure ratio of the pump $\Gamma = \frac{P_{t1}}{P_{t2}}$, the power consumption can be expressed as :

$$P = \frac{\dot{m} C_p T_{t2}}{\eta}(\Gamma^{\frac{\gamma-1}{\gamma}} - 1) \tag{27}$$

The power consumption can be expressed as a power coefficient below:

$$P_c = \frac{P}{\frac{1}{2}\rho_\infty V_\infty^3 S} \tag{28}$$

In this research, the CFJ pumping efficiency is set to 100% to calculate the power required to drive the flow. Eq. (27) indicates that the power required by the CFJ is determined linearly by the mass flow rate and exponentially by the total pressure ratio. Large injection slots reduce the power required because the total pressure loss is substantially reduced. The most efficient way to implement the CFJ is therefore to employ a large mass flow rate and low total pressure ratio.

2.4.4 Jet Momentum Coefficient

The jet momentum coefficient C_μ is a parameter used to quantify the injection jet intensity. It is defined as:

$$C_\mu = \frac{\dot{m} V_j}{\frac{1}{2}\rho_\infty {V_\infty}^2 S} \tag{29}$$

where $\dot{m}$ is the injection mass flow, V_j the injection velocity, ρ_∞ and V_∞ denote the freestream density and velocity, and S is the reference area.

To achieve zero net mass flux with the CFJ flow control, the mass flow exiting the injection slot must be equal to the mass flow entering the suction slot, i.e. $\dot{m}_{inj} = \dot{m}_{suc}$. The prescribed jet momentum coefficient C_μ is achieved by adjusting the injection cavity total pressure. Total temperature is assumed constant during this process since the total temperature increment across the compressor is generally small. The injection and suction mass flow rates are matched by adjusting the suction cavity static pressure. The iterative process is conducted throughout the simulation until the specified momentum coefficient is reached and the injection and suction mass flow match within the acceptable tolerance, which is 0.5% for the present study.

3 2D Co-Flow Jet Cylinder

The CFJ cylinder is simulated with freestream Mach number 0.063 and Reynolds numbers ranging from 5.62×10^5 – 1.686×10^6. The geometry of the CFJ cylinder is the same as previous study [12], chosen to maximize the lift coefficient while maintaining a subsonic injection flow, in order to curb the power coefficient. The CFJ flow control is implemented by adding injection and suction slots at two streamwise locations. The injection slot has a width 1% chord vertically above the center of the cylinder, at the 12 o'clock position, and the suction slot has a width 2.5% chord located 112.5° clockwise from the injection slot. The surface between the slots is translated radially inwards to a varying degree proportional to the slot heights. This "CFJ Suction Surface Translation" (CFJ SST) is necessary for streamwise injection and suction flows. A small amount of mass flow is ingested into the trailing edge slot, pressurized and energized by an imitated micro-compressor inside the cylinder, then ejected through the injection slot tangential to the main flow.

3.1 Mesh and Boundary Conditions

The 2D multiblock structured mesh for the CFJ cylinder is constructed using an O-mesh topology in order to achieve orthogonality near wall surfaces. Shown in Fig. 4, The 93,000 cell mesh is divided into 12 domains. The computational domain for the 2D cylinder is normalized by the cylinder diameter. The first cell on the wall is placed at $y^+ \approx 1$. The far-field inlet and outlet are located 85 diameters away away from the cylinder surface. The total pressure, total temperature, and flow angle are specified at the inlet boundary. Static pressure is specified at the outlet boundary. An adiabatic non-slip wall BC is enforced on the walls of the cylinder and internal ducts.

Figure 5 shows the flow field conditions for the lowest Reynolds number case. The pumping of the CFJ micro-compressor actuator is imitated by applying a total pressure inlet BC at beginning of the injection slot and a static pressure outlet BC at the end of the suction slot. Iteration of the suction static pressure is conducted to match the suction mass flow rate to that of the injection within a tolerance of 0.5%. Simultaneously, iteration of the injection total pressure is conducted to match the injection C_μ to the target C_μ within a tolerance of 0.5%. This treatment of the injection and suction is thoroughly validated in previous work [40, 41, 34, 35, 33, 3]. The y_1^+ range given in Table 1 are representative values from a single case at which $C_\mu = 6.0$.

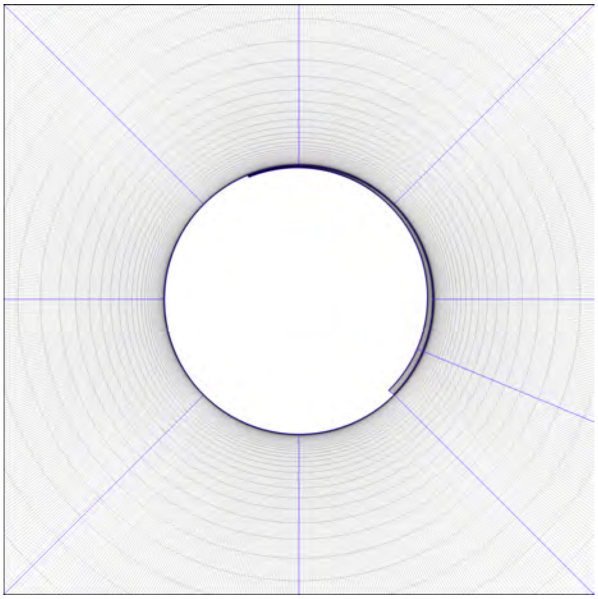

Figure 4: CFJ cylinder mesh.

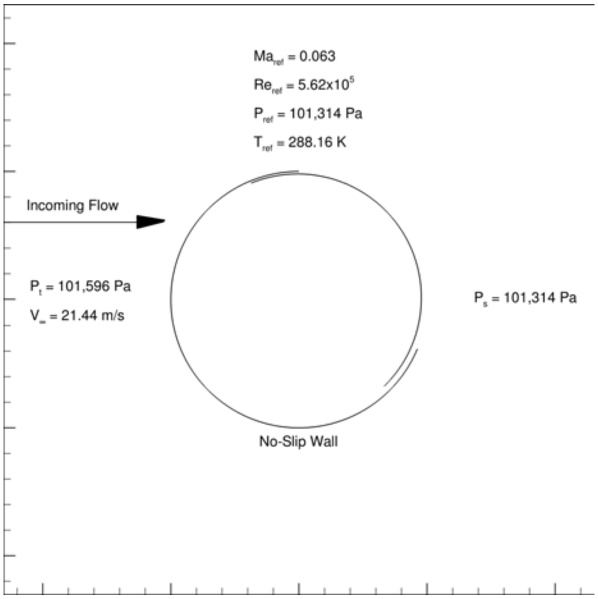

Figure 5: CFJ cylinder boundary conditions.

Table 1: CFJ Cylinder Computational Mesh Parameters

Blocks	Mesh $N_\xi \times N_\eta$	Δy_1	y_1^+
External	800×90	5.0×10^{-6}	$0.51 - 1.26$
CFJ Inj	50×60	5.0×10^{-6}	$2.02 - 2.59$
CFJ Suc	50×60	5.0×10^{-6}	$0.67 - 1.13$
CFJ SST	250×60	5.0×10^{-6}	$0.70 - 2.28$

3.2 Aerodynamic Force Coefficients

The CFJ cylinder is studied at a Mach number of 0.063. This Mach number is selected to be able to make direct comparisons to a previous study of similar CFJ cylinders [20]. Three series of simulations are conducted at Re $= 5.6 \times 10^5$, Re $= 1.1 \times 10^6$ and Re $= 1.7 \times 10^6$. The results for the three Reynolds numbers are very similar, indicating that the CFJ cylinder performance is not sensitive to Reynolds number in this range. Each series of cases is run at a range of C_μ, such that the case with the highest C_μ in each series maintains a subsonic injection jet, avoiding choked flow.

The time-averaged lift coefficient reaches a maximum $C_L = 26.72$ at $C_\mu = 2.27$. Higher C_μ are not simulated because the injection Mach number reaches 0.94. The CFJ cylinder achieves $C_L > 20$ for $C_\mu = 1.05$ and above. The two lowest C_μ cases studied in this series ($C_\mu = 0.227 - 0.273$) have unsteady results because the injection jet is not strong enough to maintain attached flow. For $C_\mu = 0.318 - 0.364$, the flow is attached, stable, and the LE and TE stagnation points are on the lower surface of the cylinder. For $C_\mu = 0.409 - 0.773$, the flow field is still stable, but the stagnation points detach from the surface, joining into a single stagnation point away from the body of the CFJ cylinder. For $C_\mu \geq 0.819$, the flow once again becomes unsteady. In Figures 6–9, the vertical bars correspond to the extrema values (e.g. $C_{L_{max}}$ & $C_{L_{min}}$) when the flow field results are unsteady. The points on the connecting line are the time-averaged value. Tabular information for each series in can be found in Section 8, Tables 9–14. Flow fields and discussion of factors contributing to the unsteady behavior are in Section 3.3.

Figure 6 shows that this CFJ cylinder produces time-averaged lift coefficients ranging 4.97 – 26.72 for the range of C_μ studied. The cases above $C_\mu = 0.455$ exceed Smith's theoretical limit of 4π for a cylinder. As the jet momentum coefficient C_μ increases, the C_L correspondingly increases due to the accelerated flow along the top surface creating a low pressure zone, as well as the high pressure zone directly below the cylinder caused by the low speed flow region. Figure 2 shows an example flow field featuring this effect. Figure 7 shows the time-averaged drag coefficients. For $C_\mu = 0.227 - 0.546$, C_D slightly decreases with increasing C_μ. As C_μ continues to increase, C_D generally increases. The minimum $C_D = 0.099$ occurs at $C_\mu = 0.546$. The maximum $C_D = 0.463$ is observed at $C_\mu = 2.274$, the highest C_μ simulated. It is clear from Figure 7 that although the time-averaged drag coefficient remains low, the oscillations in the drag coefficient are significant. The amplitude of oscillation appears to grow with increasing C_μ, to a maximum amplitude of 4.316, ranging from $C_{D_{min}} = -1.696$ to $C_{D_{max}} = 2.620$. For portions of the oscillating drag coefficient history, the CFJ produces a net negative drag, i.e. thrust.

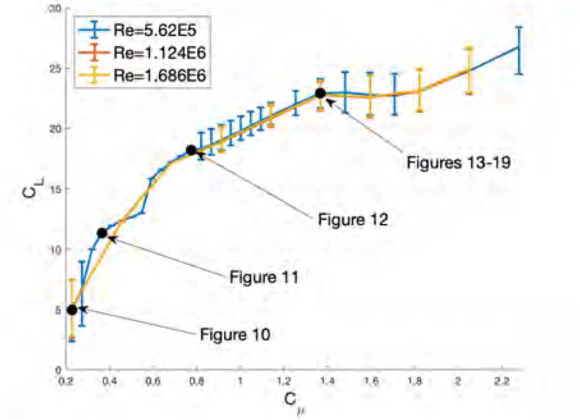

Figure 6: CFJ cylinder time-averaged lift coefficient with oscillation amplitude, Ma = 0.063

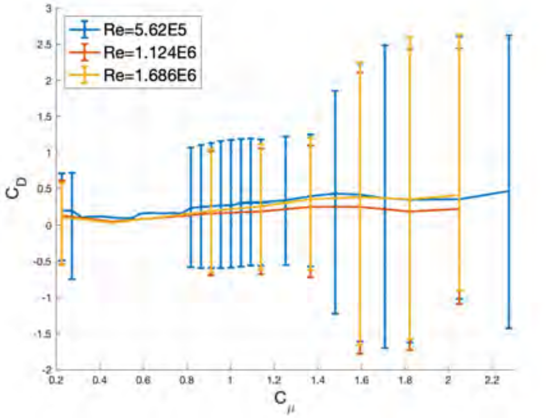

Figure 7: CFJ cylinder time-averaged drag coefficient with oscillation amplitude, Ma = 0.063

Figure 8 shows how the CFJ power required smoothly increases with C_μ. A third order polynomial describing this relationship fits this curve very well. The equation is displayed on Fig. 8, $P_c = -1.159(C_\mu)^3 + 10.924(C_\mu)^2 - 1.535(C_\mu) + 0.969$, with a coefficient of determination $R^2 = 0.999$. Figure 9 shows the CFJ cylinder's aerodynamic efficiency, corrected to account for the power required, as $(C_L/C_D)_c = C_L/(C_D + P_c)$. The peak $(C_L/C_D)_c$ occurs at $C_\mu = 0.364$. At this point, $C_L = 11.332$, $C_D = 0.119$, $P_c = 0.393$. With further increasing C_μ, the denominator grows more rapidly than the numerator, due to the nonlinear growth of P_c. For the entire range of C_μ simulated, P_c is a greater factor in the denominator than C_D.

Table 2 lists the individual contributions to the total lift coefficient for a case at $C_\mu = 1.364$. The factors listed are identified in Eqns. (21) – (24), from control volume analysis. These forces are processed at the $C_{L_{max}}$ condition. These factors are instantaneous values, not time-averaged values. Each factor oscillates in time. Table 3 similarly lists the contributions to the total drag coefficient at the $C_{L_{max}}$ condition. The surface reaction force, R', is the surface integral of the pressure and shear forces along the surface of the cylinder, excluding the surfaces

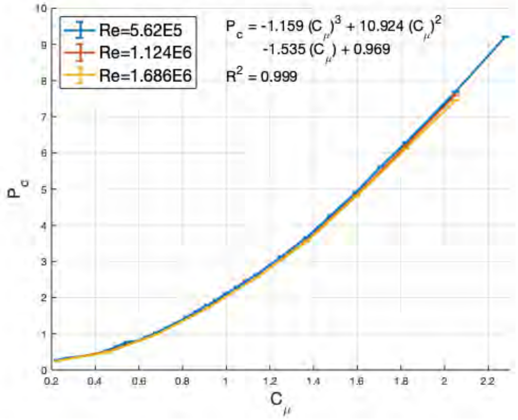

Figure 8: CFJ cylinder average power coefficient, Ma = 0.063

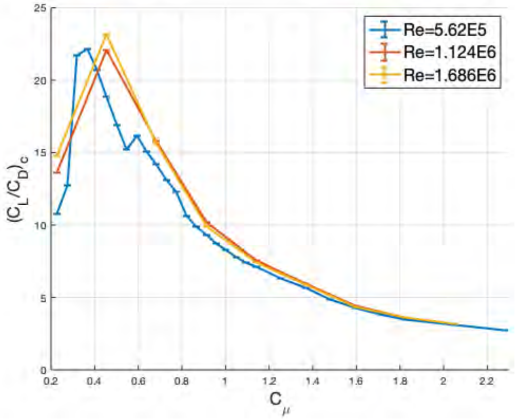

Figure 9: CFJ cylinder average corrected aerodynamic efficiency, Ma = 0.063

inside the CFJ injection and suction ducts. The force contribution of the injection and suction jets, F_{cfj}, is split into the pressure force on the slot plane, and the momentum of the flow moving through that plane.

The CFJ injection slot is perfectly horizontal, and the suction is primarily vertical. Although the net y-force contribution of the injection and suction jets seems to detract from the lift coefficient, the jets provide the means to establish the attached flow field enabling the high pressure-lift. The injection jet does produce a horizontal force of a similar magnitude and opposite sign to the drag on the surface. The sum of the oscillating drag and horizontal jet force periodically produces a net thrust.

Table 2: CFJ Cylinder $C_\mu = 1.364$ Contributions to Lift Coefficient at $C_{L_{max}}$

Cylinder Surface R'_y	32.88
Inj Jet Pressure - y	0.000
Suc Jet Pressure - y	-8.303
Inj Jet Momentum - y	0.009
Suc Jet Momentum - y	-0.536
Resultant Jet Force $F_{y_{cfj}}$	-8.830
Net C_L	24.046

Table 3: CFJ Cylinder $C_\mu = 1.364$ Contributions to Drag Coefficient at $C_{L_{max}}$

Cylinder Surface R'_x	8.764
Inj Jet Pressure - x	-3.270
Suc Jet Pressure - x	-3.434
Inj Jet Momentum - x	-1.398
Suc Jet Momentum - x	-0.188
Resultant Jet Force $F_{x_{cfj}}$	-8.290
Net C_D	0.474

3.3 Flow Field Results

In the range of C_μ studied, the CFJ cylinder can have a steady flow field, or have an unsteady, evolving flow field. For a given injection jet C_μ, the flow around the CFJ cylinder can be categorized into one of four modes. Figures 10–19 illustrate flow fields typical of each of the four modes. The four cases represented in this section are marked on the C_L versus C_μ curve, Fig. 6.

1. $C_\mu \leq 0.273,\ C_L \leq 5$: The injection jet oscillates between fully detached and partially detached. Unsteady flow field solution.
2. $0.318 \leq C_\mu \leq 0.364,\ 5 \leq C_L \leq 12$: The injection jet is fully attached. Two stagnation points exist on the lower surface of the CFJ cylinder. Stable flow field solution.
3. $0.409 \leq C_\mu \leq 0.773,\ 12 \leq C_L \leq 18$: The local flow around the entire CFJ cylinder surface is attached. The stagnation point is detached from the surface, below the CFJ cylinder. Stable flow field solution.

4. $C_\mu \geq 0.819$, $C_L \geq 18$: The local flow around the entire CFJ cylinder surface is attached. One or two stagnation points exist below the CFJ cylinder. A large vortex periodically oscillates below the cylinder.

Figure 10 shows Mach contours and streamlines of the flow at the $C_{L_{max}}$ and $C_{L_{min}}$ conditions. The injection jet does not have enough energy to overcome the adverse pressure gradient on the rear of the CFJ cylinder, and it cannot maintain attached flow. For $C_\mu = 0.227$, even at its $C_{L_{max}}$ condition, the flow separates at the trailing edge of the CFJ cylinder, before being drawn into the suction duct. Some circulation is imparted to the flow, as the leading and trailing stagnation points have moved towards the bottom of the CFJ cylinder. At its $C_{L_{min}}$ condition, the injection jet flow detaches from the trailing edge and follows the streamlines of the CFJ cylinder wake. The suction jet draws flow from the low speed wake and from flow close to the surface on the bottom of the CFJ cylinder. The stagnation points positioned at the leading edge and trailing edge of the CFJ cylinder.

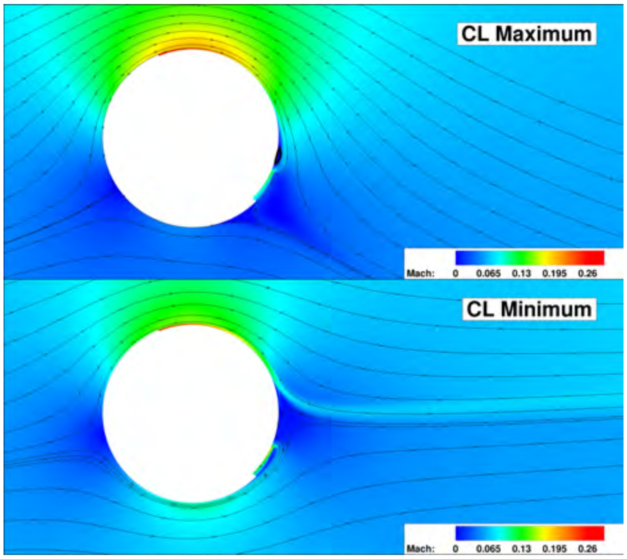

Figure 10: Unsteady CFJ cylinder flow field at $C_\mu = 0.227$, showing behavior of mode 1.

Figure 11 shows Mach contours and streamlines of the flow at $C_\mu = 0.364$. The flow field solution is steady. The CFJ injection jet has sufficient energy to attach the flow to the rear of the CFJ cylinder, although notably there remains a low-momentum region before the suction duct inlet. The flow is accelerated along the top surface of the cylinder, creating a low pressure region contributing to lift force. Due to the increased circulation of the flow, the LE and TE stagnation points have moved along the surface towards the bottom of the CFJ cylinder. This stagnation region has low speed high pressure flow, further contributing to the lift force.

Figure 12 shows Mach contours and streamlines of the flow at $C_\mu = 0.773$. The flow field solution is steady. Due to the significant energy and momentum the CFJ transfers to the flow, the circulation is greatly increased, to the point that there is no longer a stagnation point on the surface of the CFJ cylinder. A single stagnation point is positioned in the flow 1.18 diameters below the center of the CFJ cylinder, or 0.68 diameters from its bottom surface (for this specific C_μ). This stagnation point is identified by the hyperbolic saddle equilibrium point below the cylinder [42]. A single streamline bounds the local flow region, looping around the CFJ cylinder and asymptotically approaching the stagnation point. This streamline is the homoclinic loop [43], and separates the recirculating local flow from the main flow. No mass crosses this boundary, but energy and momentum are transferred from the local flow to the main flow across this boundary. As the C_μ increases, the increasing circulation moves the stagnation point farther away from the CFJ cylinder's solid body.

Figures 13–19 illustrate the periodic process for the formation and shedding of the CFJ cylinder in mode 4. This cycle of vortical wake shedding is depicted in seven distinct stages, labeled *A*–*G*. The case depicted is the

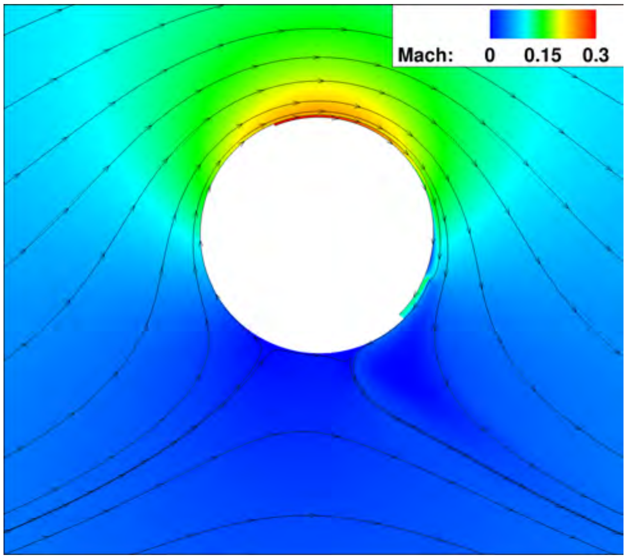

Figure 11: Steady CFJ cylinder flow field at $C_\mu = 0.364$, showing behavior of mode 2. This flow field shows the peak aerodynamic efficiency condition, $(C_L/C_D)_c = 22.148$.

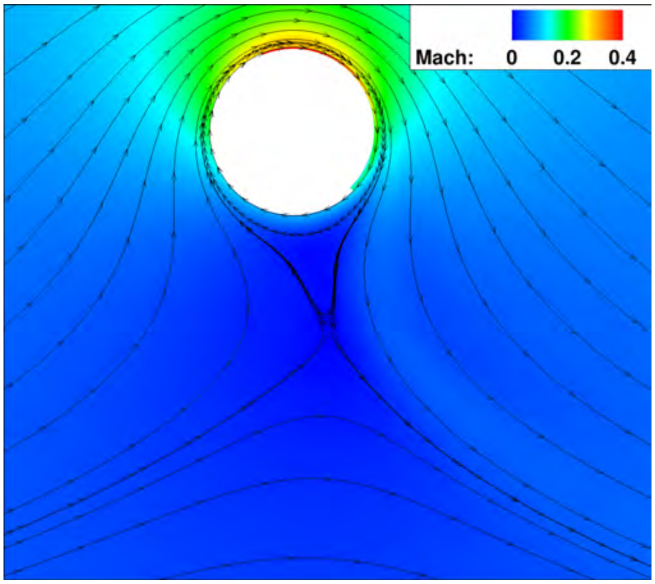

Figure 12: Steady CFJ cylinder flow field at $C_\mu = 0.773$, showing behavior of mode 3.

$C_\mu = 1.364$ condition. C_L and C_D oscillate in time as the high momentum flow from CFJ interacts with the evolving vortical flow below the cylinder body. The lift coefficient oscillates within the range 21.65 – 24.05. The drag coefficient oscillates within the range -0.57 – 1.25, with a time-averaged $C_D = 0.395$. The oscillation occurs relatively slowly, with a Strouhal number $St = 0.05$. This shedding frequency is substantially lower than the $St = 0.2$ for cylinder vortex shedding at a similar Reynolds numbers.

In Figs. 13–19, regions of each flow field with Mach number lower than 0.005 are highlighted red to more clearly indicate the presence of a stagnation point. The C_L and C_D history are superimposed on the flow field to relate the pictured flow field structure to a point on the C_L or C_D plot. These plots span 35 characteristic time, but a single period of the vortical wake shedding described in this section is 19.85 characteristic time. The vertical black line corresponds to the instant at which the flow field is plotted. An animation of this shedding process is available at (`https://youtu.be/57jKyqS0bKM`).

Figure 13 depicts the first stage of the periodic vortical wake shedding process. The cycle starts with a single hyperbolic stagnation point [42] directly below the CFJ cylinder, at a distance 1.67 diameters from the cylinder center. The high momentum flow (green) downstream of the CFJ shear layer follows an inner path along the bottom surface of the CFJ cylinder, and an outer path away from the surface, following the streamlines towards the detached stagnation point before turning back towards the leading edge of the CFJ cylinder. These diverging flow paths encapsulate a low momentum region of flow (blue) directly below the body.

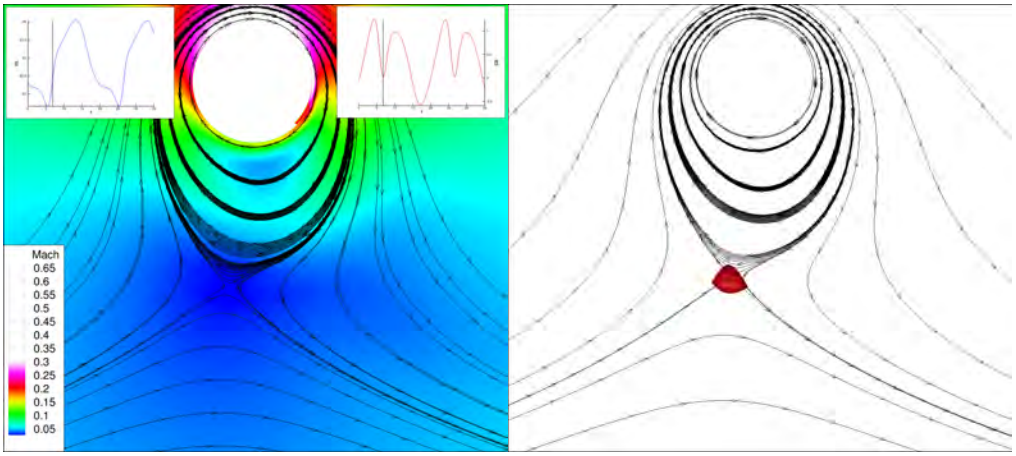

Figure 13: CFJ cylinder mode 4. $C_\mu = 1.364$. Vortical wake shedding process. Stage A.

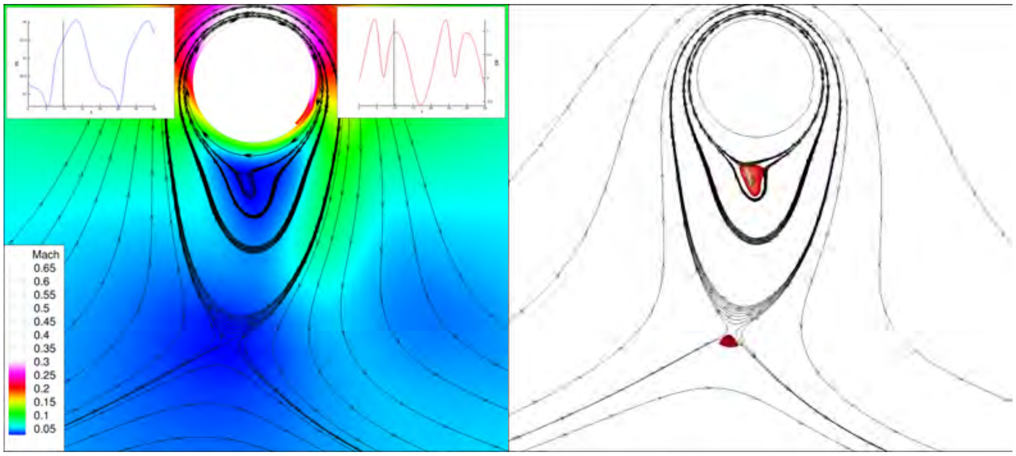

Figure 14: CFJ cylinder mode 4. $C_\mu = 1.364$. Vortical wake shedding process. Stage B.

Figure 14 depicts the second stage of the periodic vortical wake shedding process. The high momentum flow downstream of the CFJ shear layer becomes more vertical. The stagnation point pictured in Stage A moves farther from the CFJ cylinder, and the homoclinic loop surrounds a larger area below the body. Streamlines through the low momentum region bifurcate around the low speed, highest static pressure region to form a new hyperbolic stagnation point within the bounds of the local flow region. The lift climbs, while drag reaches a local maxima.

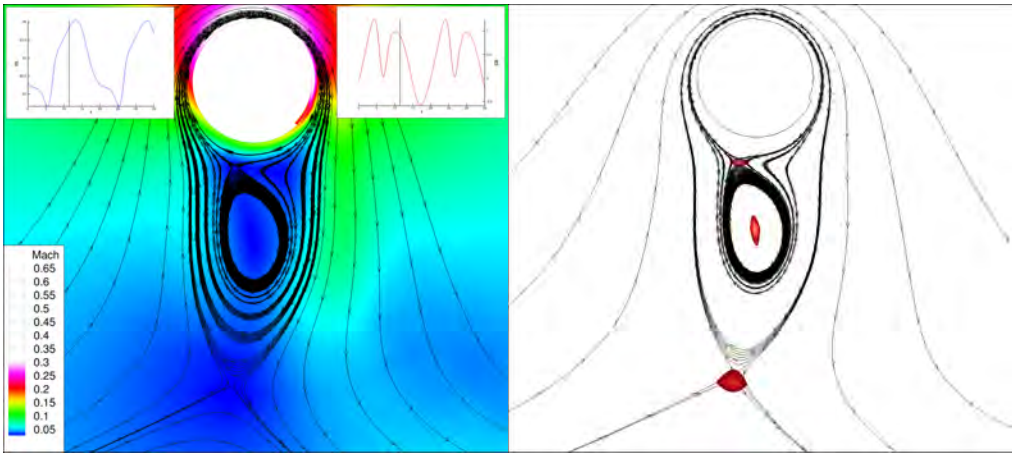

Figure 15: CFJ cylinder mode 4. $C_\mu = 1.364$. Vortical wake shedding process. Stage C.

Figure 15 depicts the third stage of the periodic vortical wake shedding process. With the formation of a second hyperbolic stagnation point, the flow field is now divided into three regions. The innermost region is bounded by the CFJ cylinder surface and the homoclinic loop through the new inner hyperbolic stagnation point. The outermost region is the main flow, which does not cross the homoclinic loop of the outer hyperbolic stagnation point. The new mesolayer is bound by the two homoclinic loops, and exists as a flow annulus. A clockwise, slowly circulating vortex grows in mesolayer between the two stagnation points. Both the high momentum jet wake flow and the now-vertical incoming main flow transfer angular momentum across the outer homoclinic loop to add clockwise vorticity to this vortex. The center of this vortex is a center equilibrium point, or a center stagnation point [43]. The center of this large vortex moves away from the cylinder, towards the lower stagnation point. The lift continues to increase, while the drag begins to decrease.

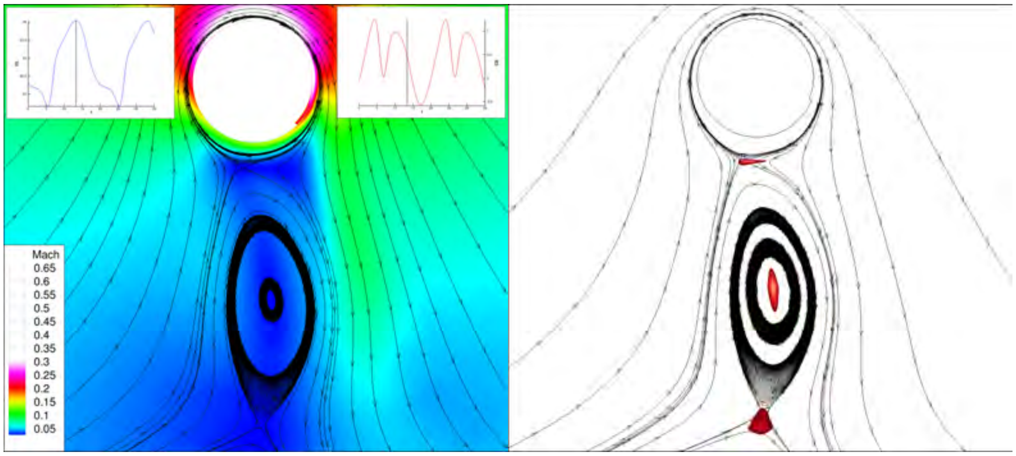

Figure 16: CFJ cylinder mode 4. $C_\mu = 1.364$. Vortical wake shedding process. Stage D.

Figure 16 depicts the fourth stage of the periodic vortical wake shedding process. At the moment when the large vortex spans the entire distance between the hyperbolic stagnation points, these stagnation points are positioned directly below the cylinder. The far stagnation point reaches its maximum extent 2.3 diameters from the cylinder surface. The near stagnation point is 0.205 diameters from the cylinder surface. The peak lift occurs at this point.

Figure 17 depicts the fifth stage of the periodic vortical wake shedding process. Once the far stagnation point reaches its maximum extent, the flow in the bottom half of the clockwise vortex does not have the energy to oppose the main flow. It is overcome by the main flow, reversing direction. The streamlines along the bottom of the vortex no longer approach a stagnation point. The center stagnation point of the vortex becomes a cusp in the flow. Streamlines above this cusp flow between the inner (now only) hyperbolic stagnation point and the cusp itself. Streamlines below the cusp never approach the CFJ airfoil. The high momentum jet wake is deflected towards the right by the expanding high pressure zone. This high momentum flow now provides a thrusting force, giving rise to a net negative drag.

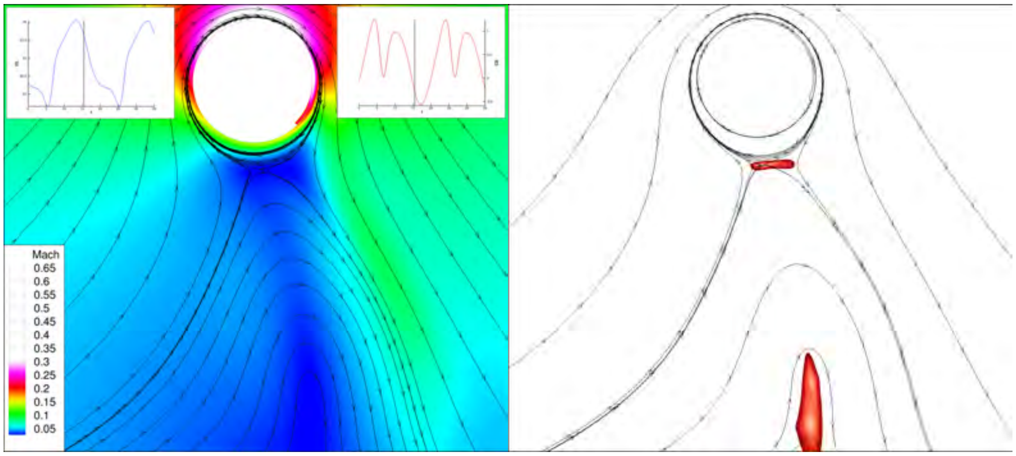

Figure 17: CFJ cylinder mode 4. $C_\mu = 1.364$. Vortical wake shedding process. Stage E.

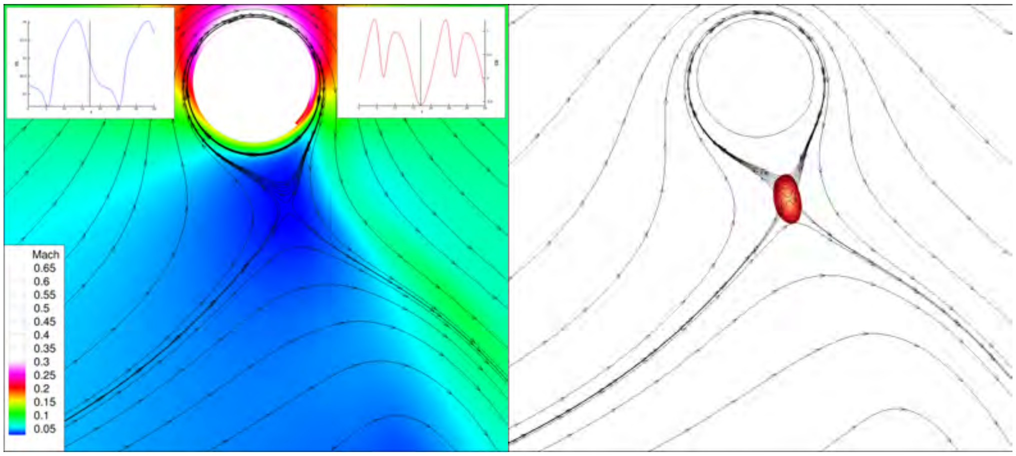

Figure 18: CFJ cylinder mode 4. $C_\mu = 1.364$. Vortical wake shedding process. Stage F.

Figure 18 depicts the sixth stage of the periodic vortical wake shedding process. As the remaining hyperbolic stagnation point moves away from body and to the right, the streamlines begin to pinch below the cylinder. The drag reaches its minimum as the high pressure region below the CFJ cylinder shifts to the right, and as the deflected jet wake is deflected to its maximum horizontal extent.

Figure 19 depicts the seventh and final stage of the periodic vortical wake shedding process. The high momentum flow from the jet wake is directed under the cylinder once again, causing the stagnation point to move upstream and slightly farther away from the body. The drag climbs to its maximum as the high momentum flow reverses its horizontal direction. Lift also reaches its minimum as the high-momentum jet wake is directed horizontally instead of vertically.

After this final stage, the stagnation point settles into its initial position directly below the cylinder and the cycle restarts from Stage A. The lift climbs rapidly and drag drops to a local minima.

The CFJ's streamwise favorable pressure gradient along the leading edge is several times that of the baseline

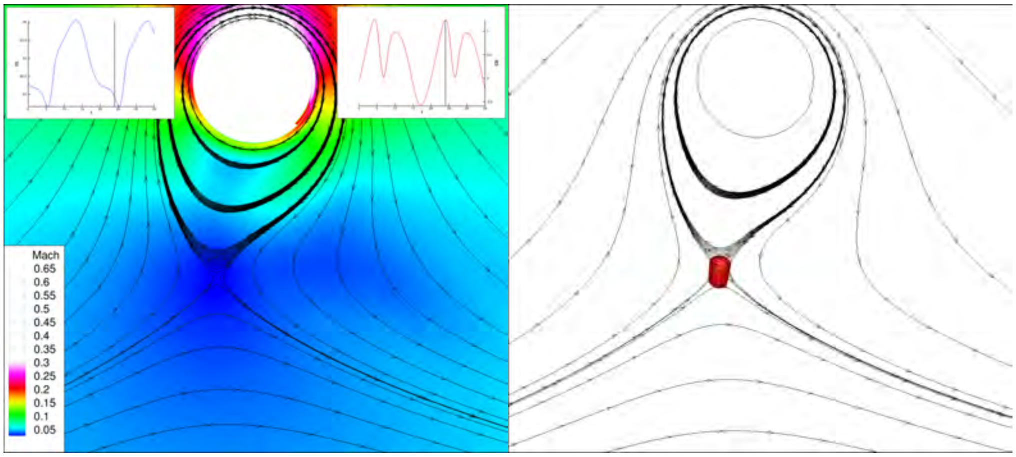

Figure 19: CFJ cylinder mode 4. $C_\mu = 1.364$. Vortical wake shedding process. Stage G.

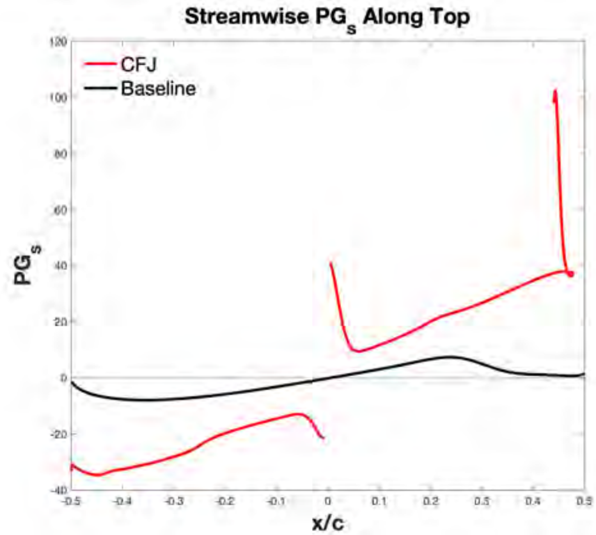

Figure 20: CFJ cylinder streamwise pressure gradient distribution.

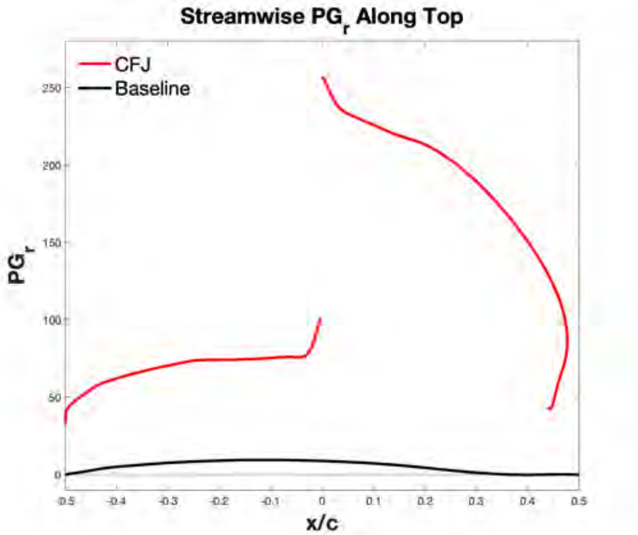

Figure 21: CFJ cylinder centrifugal pressure gradient distribution.

cylinder's. The sudden drop in PG_s just before the top of the cylinder is caused by the injection wall jet augmenting the local favorable pressure gradient due to momentum transfer from the jet to the upstream main flow. Just before the injection slot opening, we observe a very high streamwise adverse pressure gradient $PG_s = 92.2$, about 12.5 times that of the baseline cylinder at the same position. The APG rapidly falls off moving away from the mouth of the injection slot, but as we continue along the rear surface of the cylinder, the APG steadily climbs while the flow on the rear surface of the cylinder remains attached. The APG reaches a magnitude about the same as the injection opening just before the rear-most point of the cylinder (3 o'clock). The streamwise APG along the wall continues to climb rapidly as the flow passes the rear-most point, into the mouth of the suction slot, where it peaks at a value of $PG_s = 102.4$.

The radial pressure gradient coefficient for both the baseline and CFJ cylinders is adverse along the entire surface. The baseline cylinder has a maximum PG_r of 9.48. The CFJ cylinder shows an EAPG rising along the leading edge, and jumping to a maximum value of $PG_r = 257.1$ immediately after the jet injection. The flow remains attached to the rear surface of the cylinder while the radial pressure gradient decreases moving towards

Table 4: CFJ cylinder pressure gradients

Case	C_μ	C_L	$PG_{s\ max}$	$PG_{r\ max}$	PGR_s	PGR_r
Baseline	-	0.000	7.34	9.48	-	-
CFJ	1.364	22.892	102.4	257.1	13.95	27.12

the suction location, but remains adverse along the entire surface. The radial pressure gradient is non-zero at the leading edge of the CFJ cylinder because there is no stagnation point at this location.

3.3.1 Relationship Between Curvature and Radial Pressure Gradient

The inviscid, steady-state momentum equation for both compressible and incompressible fluids is given by:

$$(\mathbf{u} \cdot \nabla)\mathbf{u} = -\nabla p/\rho \tag{30}$$

where $\mathbf{u}$ is the velocity magnitude. The momentum equation can be expanded to the form:

$$u\frac{\partial(u\hat{\mathbf{s}})}{\partial s} = -\frac{1}{\rho}(\hat{\mathbf{s}}\frac{\partial p}{\partial s} + \hat{\mathbf{r}}\frac{\partial p}{\partial r}) \tag{31}$$

where $\hat{\mathbf{s}}$ is a unit vector tangent to the streamline, and $\hat{\mathbf{r}}$ is an outward-pointing unit vector pointing in the direction outward from the local center of curvature of a streamline, which itself is normal to the streamline [44]. The components of fluid acceleration along the streamline and normal to the streamline are derived from the two terms in Eq. 31. The streamwise acceleration is determined by the streamwise pressure gradient as such:

$$u\frac{\partial(u)}{\partial s} = -\frac{1}{\rho}\frac{\partial p}{\partial s} \tag{32}$$

The normal component of the acceleration is a consequence of changes in the direction of the velocity. The unit vector $\hat{\mathbf{r}}$ cannot have changes in magnitude, so its changes must be in its direction. The component of the pressure gradient normal to the streamline is given by:

$$\rho\frac{u^2}{r_c} = \frac{\partial p}{\partial r} \tag{33}$$

which is the centripetal acceleration, with r_c as the local radius of curvature. Therefore streamline curvature is associated with a component of the pressure gradient force normal to the streamlines and pointing toward the local center of curvature. Thus the radial pressure gradient is a phenomenon arising as a consequence of inviscid flow's need to turn the streamlines. The streamwise pressure gradient on the other hand is ultimately caused by changes in the velocity magnitude from viscous phenomenon like transport of energy, momentum, and shear stress.

The radius of curvature and the surface curvature are a reciprocal pair. The r_c along the outer surfaces of the CFJ cylinder is 0.5C, and in the CFJ translation region between the injection and suction slots, it is 0.4825C.

$$\kappa = \frac{1}{r_c} \tag{34}$$

4 2D Co-Flow Jet Airfoil

The CFJ and baseline airfoils are simulated at a freestream Mach number of 0.063 and Reynolds number of 5.62×10^5. Previous studies of the 2D CFJ airfoil have demonstrated lift coefficients far in excess of the theoretical limit dictated by Eq. 1 [3, 2, 45, 10]. The CFJ6421-SST150-SUC247-INJ152 airfoil geometry used in this study is a slight modification to similar airfoils studied in the past. The injection slot is widened 30% and injection duct curvature reduced to accommodate subsonic injection flow at high C_μ and very advanced angles of attack. This paper presents results from a range of C_μ at 65° AoA, to reflect the conditions of previous work [12]. The CFJ mechanism is implemented via an internal pump in the same manner as the CFJ cylinder. Results of $C_\mu = 0.568 - 2.729$ are presented in Table 15. An angle of attack study at Mach = 0.063 and Re = 5.62×10^5 finds that the NACA6421 airfoil reaches $C_{L_{max}}$ at 15.5° AoA, shown in Fig. 22. Pressure gradient results are compared to the 2D baseline NACA6421 airfoil at 15.5° AoA. Figure 23 shows Mach contours of the baseline NACA6421 airfoil at its 15.5° AoA. At this AoA the baseline airfoil possesses the highest adverse pressure gradient.

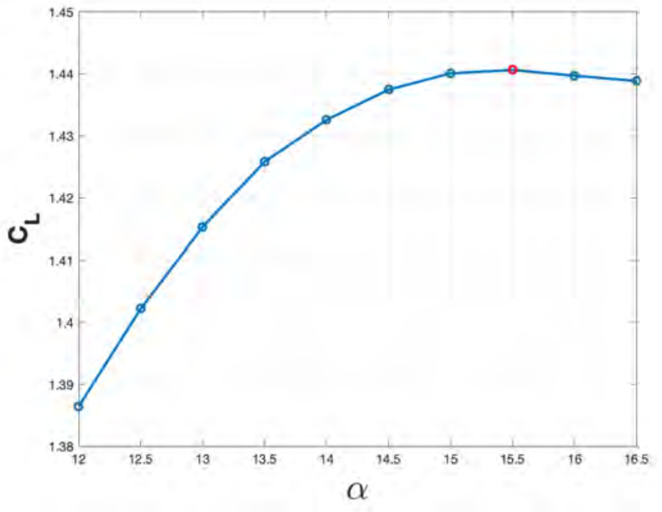

Figure 22: Baseline airfoil C_L vs AoA.

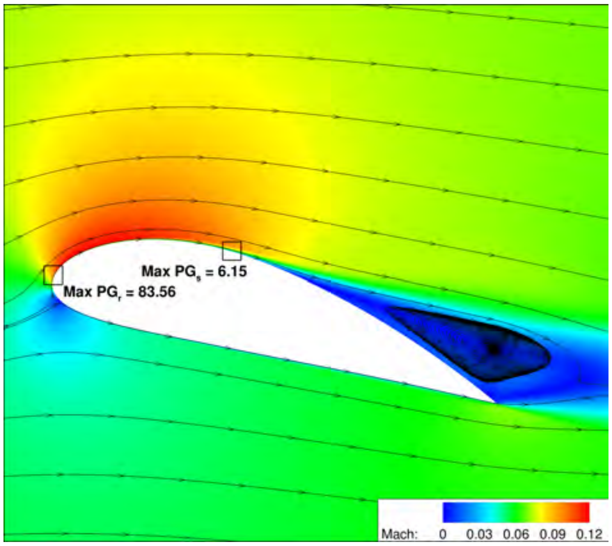

Figure 23: Baseline NACA6421 airfoil, $\alpha = 15.5°$.

4.1 Mesh and Boundary Conditions

The 2D multiblock structured mesh for the CFJ airfoil is constructed using an O-mesh topology in order to achieve orthogonality near wall surfaces. Shown in Fig. 24, the 365,000 cell mesh is divided into 78 domains. The computational domain for the 2D airfoil is normalized by the airfoil chord. The freestream flow conditions and boundary conditions are illustrated in Fig. 25. The far-field inlet and outlet are located 200 chords away from the airfoil surface. The total pressure, total temperature, and flow angle are specified at the inlet boundary. Static pressure is specified at the outlet boundary. A non-slip adiabatic wall BC is enforced on the walls of the airfoil and internal ducts. The pumping of the CFJ micro-compressor actuator is imitated by applying a total pressure inlet BC at beginning of the injection slot and a static pressure outlet BC at the end of the suction slot. Iteration of the suction static pressure is conducted to match the suction mass flow rate to that of the injection within a tolerance of 0.5%. Simultaneously, iteration of the injection total pressure is conducted to match the injection C_μ to the target C_μ within a tolerance of 0.5%. This treatment of the injection and suction is thoroughly validated in previous work [40, 41, 34, 35, 33, 3]. The y^+ range given in Table 5 are taken from the $C_\mu = 2.729$ case.

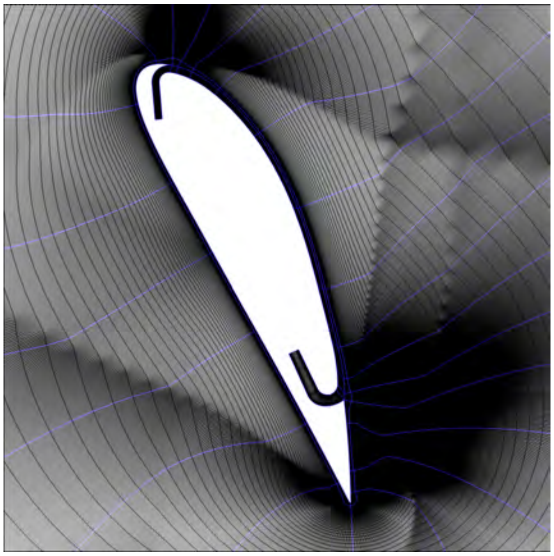

Figure 24: CFJ6421 computational mesh

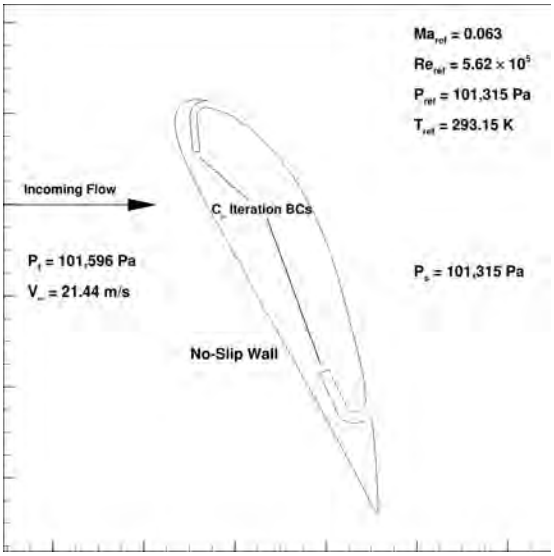

Figure 25: CFJ6421 boundary conditions

Table 5: CFJ Airfoil Computational Mesh Parameters

Blocks	Mesh $N_\xi \times N_\eta$	Δy_1	y_1^+
External	2000 × 300	5.0×10^{-6}	0.01 – 2.93
CFJ Inj	80 × 60	6.0×10^{-7}	0.16 – 0.49
CFJ Suc	80 × 60	6.0×10^{-7}	0.01 – 0.92
CFJ SST	800 × 60	6.0×10^{-7}	0.12 – 0.74

4.2 Flow Field Results

The CFJ airfoil was studied at a freestream Mach number of 0.063, and Reynolds number 5.62×10^5, to mirror the conditions of the CFJ cylinder. The CFJ C_μ ranged from $0.568 - 2.729$. Higher C_μ results are not included in this paper because the injection jet reaches supersonic conditions for higher C_μ. Tabular results for this series of cases are presented in Table 15, and plots of select results are shown below. For $C_\mu = 0.568 - 0.682$, the injection jet does not supply enough momentum and energy to attach the main flow. Significant wake shedding occurs behind the airfoil causing the lift and drag coefficients to oscillate. The maximum and minimum lift and drag coefficients are denoted by the vertical bars in Figs. 26 and 27. Interestingly, at $C_\mu = 0.796$, the flow field settles into a stable solution despite the main flow detaching from the lower half of the suction surface. In this flow field, a vortex forms in the wake of the airfoil, downstream of the injection slot. For $C_\mu \geq 1.137$, the CFJ supplies sufficient mixing to attach the main flow to the entire suction surface of the airfoil.

A stronger injection jet adds more circulation to the flow field. As the circulation increases, the leading edge stagnation point moves down along the pressure surface towards the sharp airfoil tail. The trailing edge stagnation point stays at the tail for all C_μ simulated. For $C_\mu \geq 2.274$, a new set of stagnation points form in the flow field. A circulating region of flow forms just under the airfoil, induced by the shear from the high-momentum jet wake flow. The farthest point of this circulating region forms a detached stagnation point in the flow field, identifiable by the hyperbolic saddle formed by the streamlines. A high C_μ jet induces a stronger, more influential vortex in this region, and the detached stagnation point moves farther from the airfoil body. This vortex is stationary relative to the airfoil. It can be said that this vortex forms a "virtual extension" of the airfoil surface, acting like a flap to increase C_L and C_D [3].

Unlike the CFJ cylinder, one stagnation point remains on the surface of the airfoil for the entire C_μ range simulated. The streamlines around the airfoil do not form a closed loop near the surface like they did for the cylinder. Figure 37 shows the streamlines around the CFJ airfoil for $C_\mu = 2.729$. Compare the flow topology to Fig. 12, which shows the CFJ cylinder at $C_\mu = 0.773$. The CFJ airfoil maintains a stagnation point on the surface even with a much higher injection jet power tan the CFJ cylinder. The airfoil has a greater eccentricity than the cylinder and a sharp trailing edge. Naturally it requires greater circulation to turn the flow around the sharper edges. The minimum circulation required to turn the flow around the airfoil's sharp trailing edge without detaching from the surface is likely impractically high.

Figure 26 shows the CFJ airfoil's time-averaged lift coefficients ranging 3.57 to 13.41. For $C_\mu \leq 0.682$, the CFJ does not supply sufficient energy to the flow to overcome the adverse pressure gradient. The injection wall jet oscillates between fully attached and partially attached. For $C_\mu \geq 0.796$, the flow field is steady. As the jet momentum coefficient C_μ increases, C_L increases due to the "Super-Suction" effect of the accelerated flow around the airfoil's leading edge, as well as the higher pressure from the stagnation region below the airfoil's tail. The cases with $C_\mu > 1.137$ exceed Smith's theoretical limit of $C_{L_{max}} = 7.6$ for a 21% thickness airfoil [16], thus we describe those cases as having a Super-Lift Coefficient. Figure 27 shows the time-averaged drag coefficient, which ranges 1.467 to -0.097. The two lowest C_μ cases with massive separation understandably have significantly higher drag than the cases with steady, well-attached flow. C_D decreases with increasing C_μ. For $C_\mu \geq 1.592$, the CFJ horizontal jet force outweighs the airfoil aerodynamic drag to produce a net negative drag, i.e. thrust.

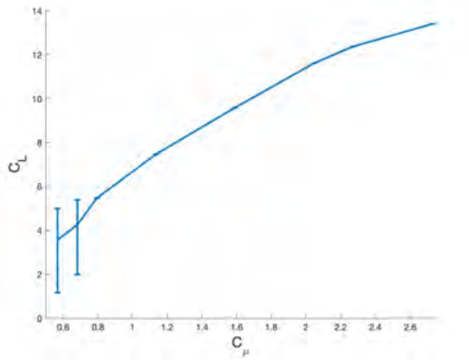

Figure 26: CFJ airfoil lift coefficient.

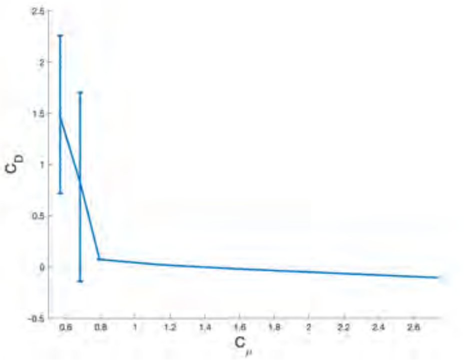

Figure 27: CFJ airfoil drag coefficient.

Figure 28 shows how the CFJ power required smoothly increases with C_μ. A third order polynomial describing this relationship fits this curve very well. The equation is displayed on Fig. 28, $P_c = 0.7600(C_\mu)^3 - 0.0569(C_\mu)^2 + 2.6881(C_\mu)+0.3165$, with a coefficient of determination $R^2 = 0.9998$. Figure 29 shows the CFJ airfoil's aerodynamic efficiency, corrected to account for the power required, as $(C_L/C_D)_c = C_L/(C_D + P_c)$. The peak $(C_L/C_D)_c$ occurs at $C_\mu = 0.796$. At this point, $C_L = 5.463$, $C_D = 0.074$, $P_c = 0.524$. With further increasing C_μ, the denominator grows much more rapidly than the numerator, due to the nonlinear growth of P_c. Excepting the two lowest C_μ cases with massively separated flow, P_c is always a much greater factor in the denominator than C_D. Fig. 29 seems to indicate that for a CFJ airfoil at very high angle of attack, the peak efficiency occurs at the minimum C_μ required to attach the main flow around the leading edge of the airfoil.

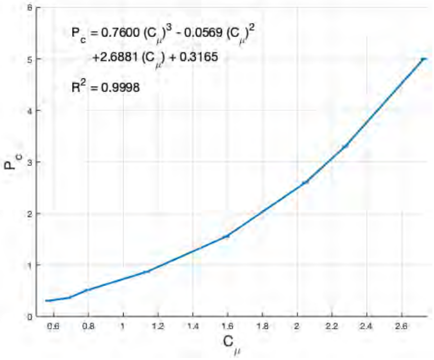

Figure 28: CFJ airfoil average power coefficient.

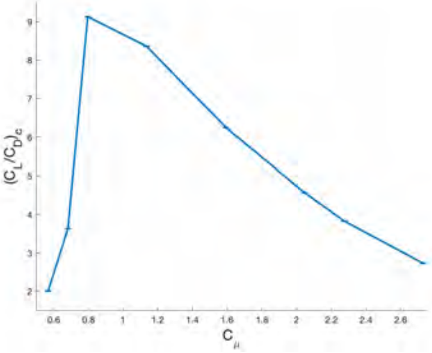

Figure 29: CFJ airfoil average corrected aerodynamic efficiency.

Table 6 lists the individual contributions to the total lift coefficient for the case at $C_\mu = 2.729$. The factors listed are identified in Eqns. 21 – 24, from control volume analysis. Table 7 lists the contributions to the total drag coefficient. The surface reaction force, R', is the surface integral of the pressure and shear forces along the surface of the airfoil, excluding the surfaces inside the CFJ injection and suction ducts. The force contribution of the injection and suction jets, F_{cfj}, is split into the pressure force on the slot plane, and the momentum of the flow moving through that plane.

Although the net y-force contribution of the injection and suction jets seems to detract from the lift coefficient, the jets are essential to the CFJ system, because they provide the means to establish the EAPG and maintain attached flow, enabling the high lift. The injection jet does produce a horizontal force of a similar magnitude and opposite sign to the drag on the surface. At this C_μ, the net horizontal force is negative, indicating that the system is producing thrust.

Table 6: CFJ Airfoil $C_\mu = 2.729$ Contributions to Lift Coefficient

Airfoil Surface R'_y	18.621
Inj Jet Pressure - y	1.373
Suc Jet Pressure - y	-5.665
Inj Jet Momentum - y	0.250
Suc Jet Momentum - y	-1.168
Resultant Jet Force $F_{y_{cfj}}$	-5.210
Net C_L	13.411

Table 7: CFJ Airfoil $C_\mu = 2.729$ Contributions to Drag Coefficient

Airfoil Surface R'_x	15.167
Inj Jet Pressure - x	-4.236
Suc Jet Pressure - x	-7.253
Inj Jet Momentum - x	-2.822
Suc Jet Momentum - x	-0.954
Resultant Jet Force $F_{x_{cfj}}$	-15.264
Net C_D	-0.097

Figures 36–35 display Mach contours and streamlines for the CFJ airfoil cases studied. For $C_\mu \leq 0.682$, the CFJ does not supply sufficient energy to the flow to overcome the adverse pressure gradient and maintain attached flow. The injection wall jet oscillates between fully attached and partially attached. The wake of the airfoil is massively separated, appearing like blunt body flow separation. The instantaneous flow field of Fig. 30 shows large-scale vortex shedding downstream of the airfoil. For $C_\mu \geq 0.796$, the flow field is steady.

For $C_\mu = 0.568 - 2.056$, the airfoil's leading edge stagnation point is positioned on the airfoil's pressure surface. With increasing C_μ, the CFJ imparts increasing circulation to the flow. With increasing circulation, the LE stagnation point moves toward the trailing edge. The CFJ airfoil's influence on the flow field grows noticeably. Comparing Fig. 30 to Fig. 37, the streamlines enter and exit the image approximately horizontally for the

$C_\mu = 0.568$ case, whereas the streamlines enter and exit the image with a large vertical velocity component for the $C_\mu = 2.729$ case.

As the high velocity wake from the airfoil's suction surface meets the low velocity stagnation zone below the airfoil's trailing edge, it forms a shear layer which imparts angular momentum to the flow trapped between the leading edge stagnation point and the flow past the trailing edge. For $C_\mu \geq 2.274$, that momentum transfer is sufficient to form a large clockwise vortex positioned vertically below the airfoil trailing edge. A detached stagnation point is formed in the flow at the lower end of this vortex. With increasing C_μ, the vortex grows in strength and the detached stagnation point moves downwards, away from the airfoil surface. At $C_\mu = 2.274$, the detached stagnation point is 0.395C below the trailing edge, shown in Fig. 36. At $C_\mu = 2.729$, that distance is increased to 0.568C below the trailing edge, shown in Fig. 37. This stronger, more influential vortex extends the airfoil's influence further into the flow field, greatly increasing the circulation, and consequently C_L.

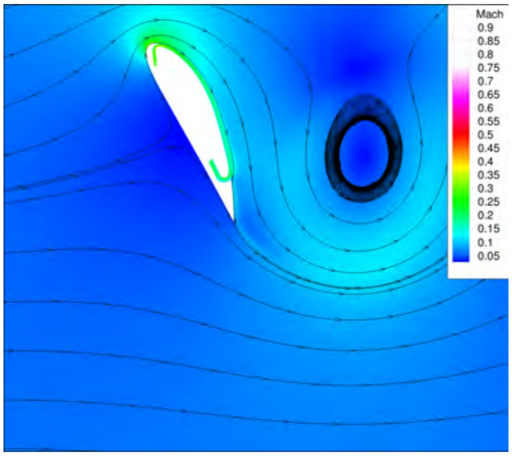

Figure 30: Inst. Mach contour, $C_\mu = 0.568$.

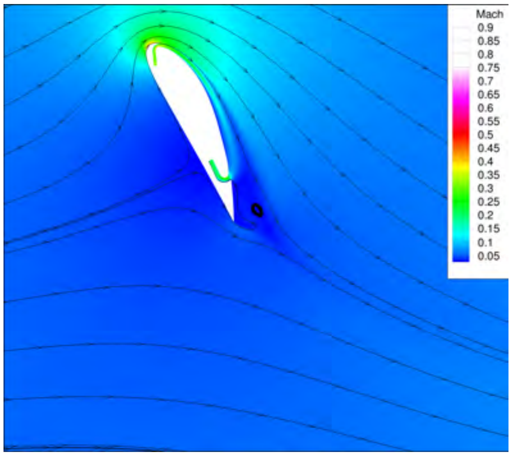

Figure 31: Inst. Mach contour, $C_\mu = 0.682$.

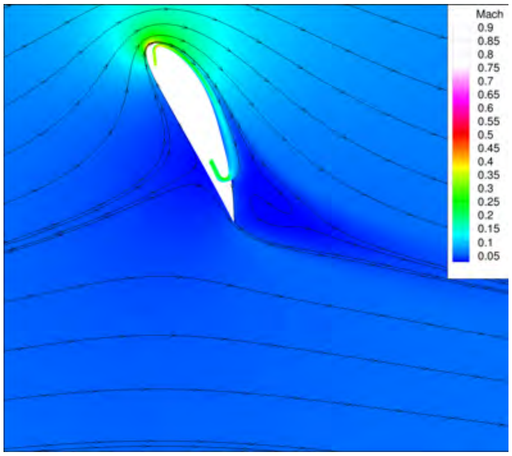

Figure 32: Mach contour, $C_\mu = 0.796$.

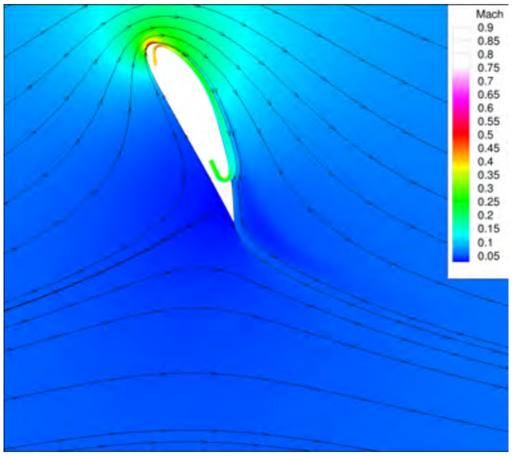

Figure 33: Mach contour, $C_\mu = 1.137$.

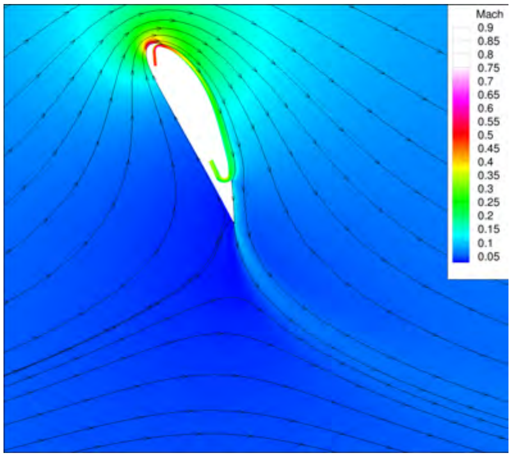

Figure 34: Mach contour, $C_\mu = 1.592$.

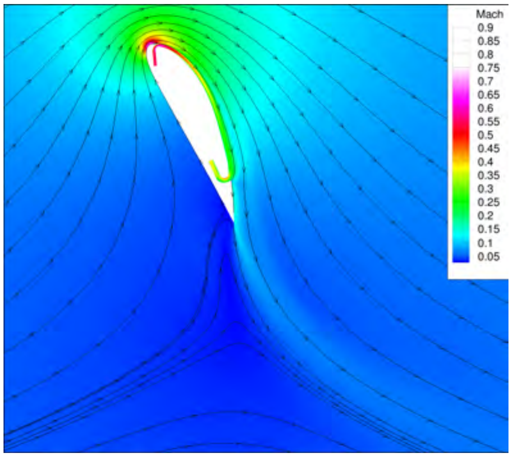

Figure 35: Mach contour, $C_\mu = 2.046$.

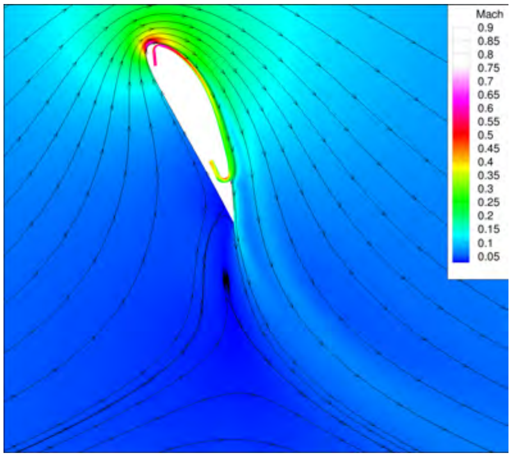

Figure 36: Mach contour, $C_\mu = 2.274$.

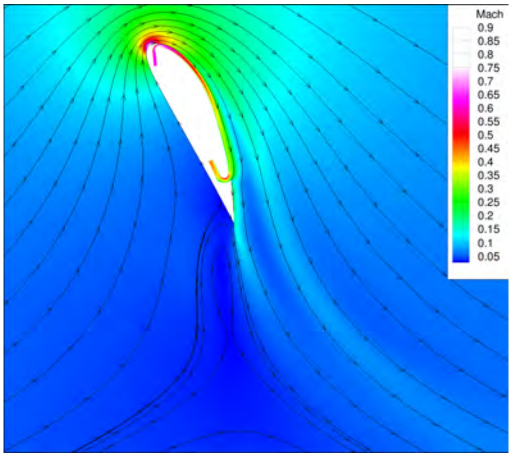

Figure 37: Mach contour, $C_\mu = 2.729$.

4.3 Pressure Gradients

In the previous section, we evaluate EAPG flow around a cylinder in order to understand the mechanisms enabling flow attachment in such conditions. We apply the same methodology to the CFJ airfoil, which we know to posses more extreme flow conditions and pressure gradients. Because the flow must turn more sharply around features of the airfoil, we observe significantly higher pressure gradients in regions with higher streamline curvature. The local radius of curvature is related to the flow angle by $1/r_c = \partial\alpha/\partial l$, so Eq. 33 can be further expanded to express the radial pressure gradient over a flow section proportional to the flow angle through which it sweeps. In this equation, α is the flow angle and l is the path length [44].

$$\frac{\partial p}{\partial r} = \rho u^2 \frac{\partial \alpha}{\partial l} \tag{35}$$

For the cases with attached flow, the streamlines transit around the leading edge by nearly 180°. For the highest C_μ case, the leading edge peak Mach number reaches 0.759, 12.05 times higher than the freestream Mach number. It generates a "super-suction" effect at the LE which contributes to the super-lift coefficient. For the cases studied in this paper, the maximum streamwise pressure gradient PG_s at the leading edge of the airfoil is roughly 256 times the magnitude of the maximum PG_s for the baseline airfoil at its max C_L condition, and the maximum centrifugal pressure gradient PG_r measured is roughly 54.4 times that of the baseline. Such a high resilience to the extreme adverse centrifugal pressure gradient without detaching the flow must be attributed to the induction effect of the CFJ jet injection located downstream.

The CFJ6421 airfoil shows the ability to add significant circulation to the flow field, generating lift far beyond the limit set in Eq. 1. This creates an EAPG around the LE of the airfoil and down the length of the suction surface. The CFJ airfoil overcomes extreme adverse pressure gradients to maintain attached flow along its entire suction surface for angles of attack far beyond what a baseline airfoil could manage. Unlike the cylinder, which has a favorable pressure gradient along the entire LE, the CFJ airfoil does not. Fig. 38 shows that at the very leading edge of the airfoil, the flow experiences a favorable streamwise pressure gradient PG_s, but it quickly rises to an adverse pressure gradient past the LE, to a peak value of 1416. The baseline NACA6421 airfoil at 15.5° displays a maximum PG_s past the LE of just 6.15. The adverse pressure gradient declines towards the injection slot. Like the CFJ cylinder, the maximum streamwise pressure gradient coefficient PG_s is observed at the location of the injection jet, with a magnitude of $PG_s = 5407$. The EAPG declines rapidly away from the injection slot, but maintains a magnitude qualifying it as an EAPG along the entire length of the suction surface transition region. The PG_r distribution is similar to the PG_s distribution. The radial adverse pressure gradient increases in strength as the flow moves towards the LE, and decreases in strength past the leading edge, peaking at 4679. The baseline NACA6421 sees a maximum PG_r of 83.56. Like the cylinder, the maximum PG_r for the CFJ airfoil is measured directly after the injection slot, with a value of 6487. The pressure field and positions of each maximum pressure gradient coefficient are labeled in Fig. 39.

Table 8: CFJ airfoil pressure gradients

Case	C_μ	C_L	$PG_{s\ LE}$	$PG_{r\ LE}$	$PG_{s\ inj}$	$PG_{r\ inj}$	PGR_s	PGR_r
Baseline	-	1.441	6.15	83.56	-	-	-	-
CFJ	12.0	13.411	1416	4679	5407	6487	879.2	77.6

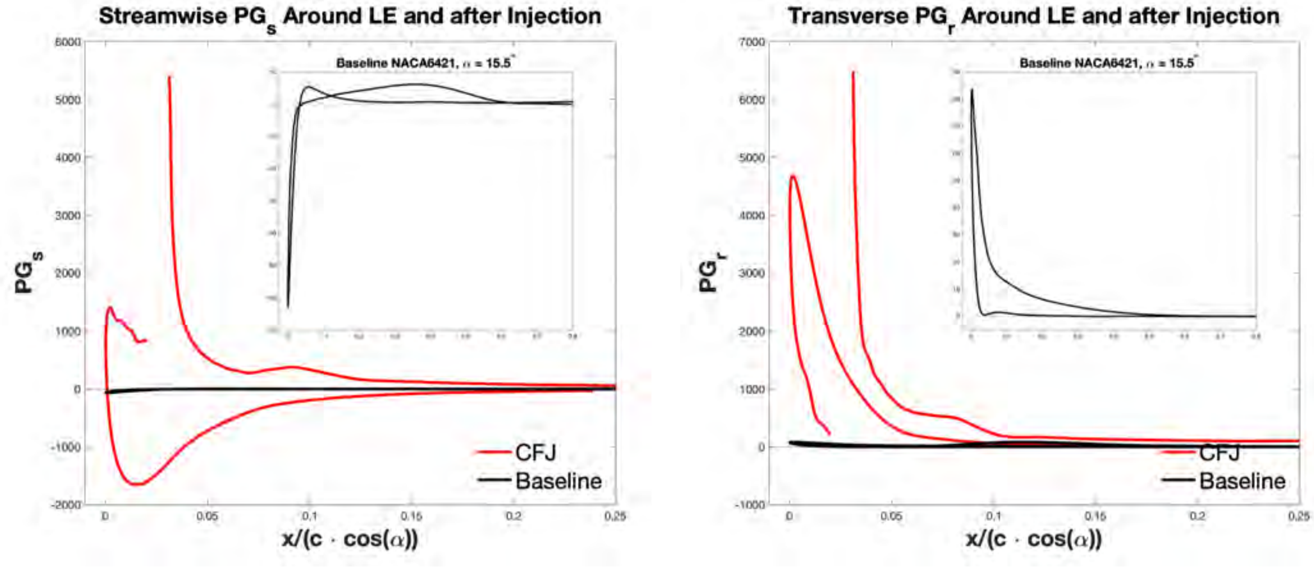

Figure 38: CFJ airfoil streamwise pressure gradient distribution (left), Radial pressure gradient distribution (right).

It should be noted that the PG_r close to the wall inside the wall jet is heavily influenced by the local radius

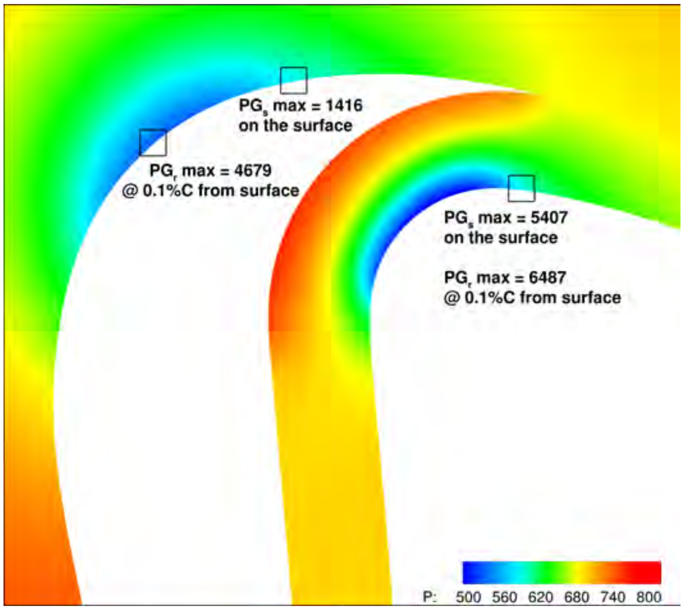

Figure 39: CFJ maximum pressure gradient locations and pressure field.

of curvature of the wall. Inside the injection duct the minimum radius of curvature is just 1.8%C, about half the radius of curvature of the airfoil leading edge. The injection duct itself is a necessary but somewhat arbitrary construction used to implement the C_μ control, turn the flow from the imagined compressor to the injection slot, and ensure a developed boundary layer as the jet enters the main flow field. This paper does not report the pressure gradients or flow attachment criteria within the injection and suction ducts. A duct with a more lower curvature would observe a somewhat lower peak PG_r. However, we note that for the cylinder the duct turning radius is as large as physically possible and still shows a tremendous PG_r at the injection location.

4.4 Flow Attachment Evaluated Using Turbulent Wall Jet Momentum Equation

Flow along the surface of the CFJ airfoil $C_\mu = 2.729$ case is numerically evaluated via the turbulent wall jet momentum equation, Eq. (4), repeated here for convenience. Four positions are selected to visualize the flow attachment term distributions, and investigate the physical mechanisms the CFJ employs to attach flow in an EAPG. Figure 40 labels the four positions on the airfoil surface. Position A is the leading edge of the airfoil. Position B is located on the airfoil surface 1%C upstream from the injection slot. Position C is on the airfoil surface 1%C downstream of the injection slot. Position D is on the airfoil surface 20%C downstream of the injection slot.

$$\rho u \frac{\partial u}{\partial x} + \rho v \frac{\partial u}{\partial y} - \frac{1}{Re}\frac{\partial \mu}{\partial y}\frac{\partial u}{\partial y} + \frac{\partial p}{\partial x} = \frac{1}{Re}\mu\frac{\partial^2 u}{\partial y^2} \tag{4 revisited}$$

Figures **??**–**??** plot the turbulent wall jet momentum equation terms for each point. The vertical axis is y^+, the dimensionless wall distance. y^+ values up to about 5 are in the viscous sublayer. y^+ values of about 5–30 are the buffer layer. y^+ values of about 30–1000 correspond to the inertial boundary layer. These plots have a maximum y^+ of 50, so they focus on a region very close to the wall.

At position A (Fig. 41), the leading edge of the airfoil, the flow has a favorable pressure gradient. The sum of

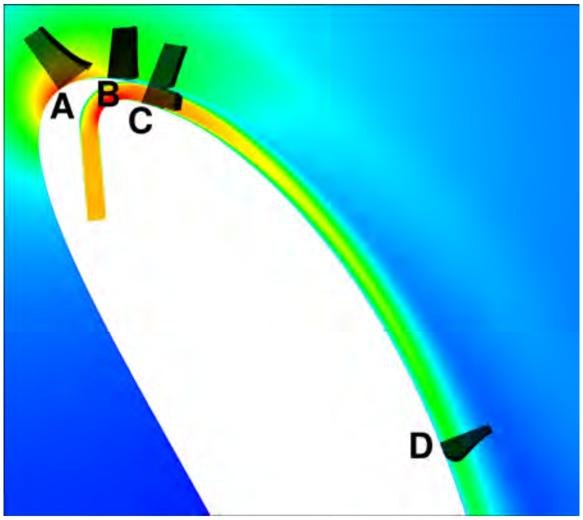

Figure 40: Positions for evaluating flow attachment.

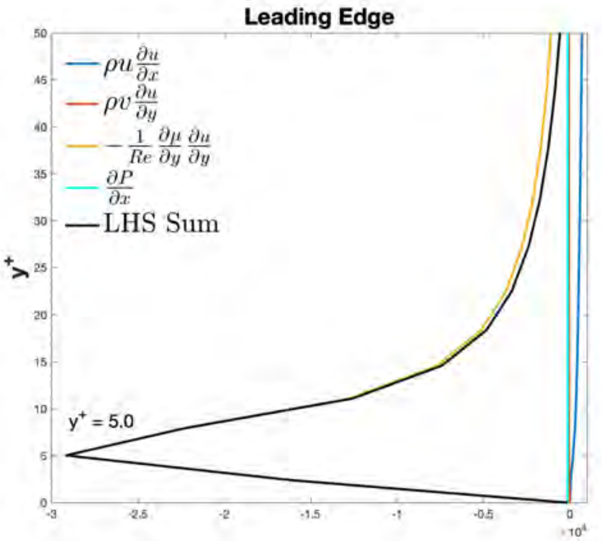

Figure 41: Position A.

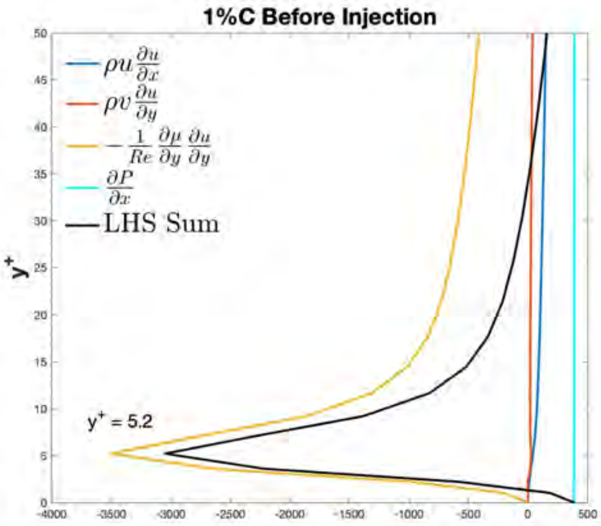

Figure 42: Position B.

the LHS of Eq. (4) is negative everywhere, and the flow is naturally attached.

At position B (Fig. 42), 1%C upstream of the injection jet, the adverse pressure gradient (cyan line) comes into play, pushing the flow towards separation. The streamwise momentum transport term, $\rho u \cdot \partial u/\partial x$ (blue line) and the transverse momentum transport term, $\rho v \cdot \partial u/\partial y$ (red line) are also slightly positive here. The LHS sum of Eq. (4) is positive on the wall (black line). The turbulence diffusion term (yellow line) grows very rapidly in the viscous sublayer. This term is solely responsible for offsetting the other terms to maintain attached flow at this position. It overwhelms the EAPG within the boundary layer, moving the sum of the LHS to be negative off the wall. At its maximum, this term is about 7 times the magnitude of the EAPG. The turbulent eddy viscosity diffusion, $\frac{1}{Re}\frac{\partial \mu}{\partial y}\frac{\partial u}{\partial y}$, plays a crucial role in maintaining flow attachment around the LE of the airfoil, but is much stronger immediately after the injection jet.

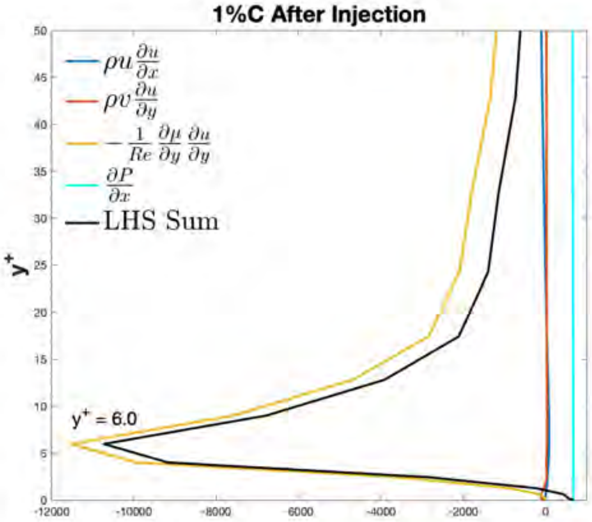

Figure 43: Position C.

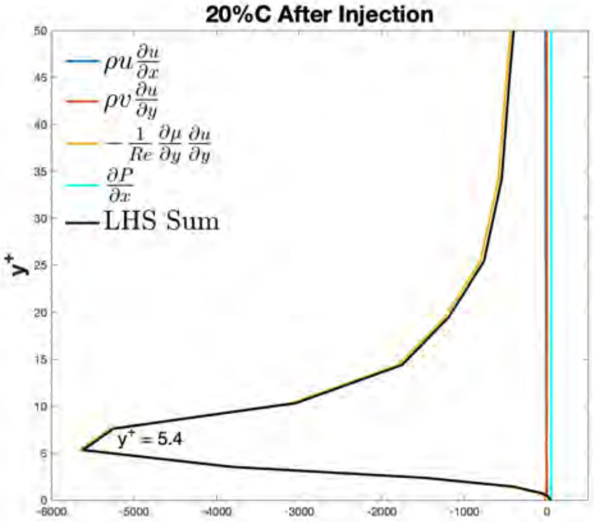

Figure 44: Position D.

At position C (Fig. 43), 1%C downstream of the injection jet, the EAPG (cyan) is the highest of the four positions evaluated. The spanwise vorticity ω_z is also highest here due to the strong vorticity flux acting on the flow from shear along the inner duct walls. The turbulent eddy viscosity diffusion is incredibly strong here, reaching a magnitude about three times greater than position B. The turbulent eddy viscosity diffusion term again easily overpowers the APG and maintains a negative LHS sum within the boundary layer.

At position D (Fig. 44), 20%C downstream of the injection jet, the turbulent eddy viscosity diffusion term tapers in strength by about 50%, but so does the adverse pressure gradient. The clockwise vorticity from the wall jet is more than enough to maintain flow attachment.

Looking at these four figures, it is clear that for the CFJ in an EAPG, the the turbulent eddy viscosity diffusion term is dominant for energizing the boundary layer to sufficiently overcome the adverse pressure gradient and maintain attached flow. This term is also most responsible for transporting momentum and energy from the CFJ injection jet to the adjacent main flow, influencing attachment upstream of the injection jet as well as downstream.

5 Validation of Mesh Independence and RANS Models

Two validation simulations of the CFJ cylinder $C_L = 22.89$ case were conducted using our in-house CFD program, FASIP. The first case quadrupled the number of cells, maintaining the same wall spacing. The second case halved the physical time step used in the time marching scheme. Fig. 45 shows that the converged lift and drag history of these two cases are virtually identical to those of the CFJ cylinder case.

Since RANS models may not be developed for EAPG flows, using a different RANS model may validate the results to ensure they are within the RANS assumptions. The cases in this paper use the Spalart-Allmaras One-Equation Model with the original weights proposed in 1992 [21]. This model was designed to solve wall-bounded flows, and has been widely adopted for aerospace applications. However, the flow conditions in an EAPG may fall outside of the calibration range for this model. The S-A model solves a modeled transport equation for the kinematic eddy turbulent viscosity — the very same term that we identify as being almost solely responsible for maintaining attached flow in an EAPG.

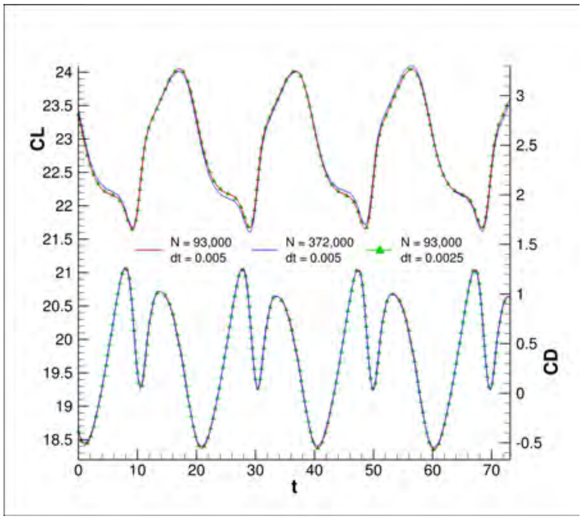

Figure 45: S-A model validation cases.

To validate the S-A model for the EAPG flows, the CFJ cylinder $C_L = 22.89$ case is computed with the k-ω SST turbulence model [46], which was implemented and validated in FASIP by Patel and Zha [47]. We choose the the two equation k-ω Shear Stress Transport model for two reasons. First, the k-ω SST model has been shown to provide an accurate prediction of flow separation and turbulent behavior in adverse pressure gradients due to computing the specific rate of turbulence dissipation by an additional transportation equation. Second, the k-ω SST model combines the beneficial aspects offered by both the k-ϵ and k-ω models by using a blending function off the wall. It employs a k-ϵ model in the freestream where the pressure gradients are small, and then switches to a k-ω model near the wall to take advantage of the higher turbulence sensitivity of the k-ω model. This method allows for high accuracy in solving the boundary layer and local turbulent flow physics all the way to the wall [48]. The blending between the models takes place in the outer wake region, and ensures that the k-ϵ model is used to solve for free shear layers.

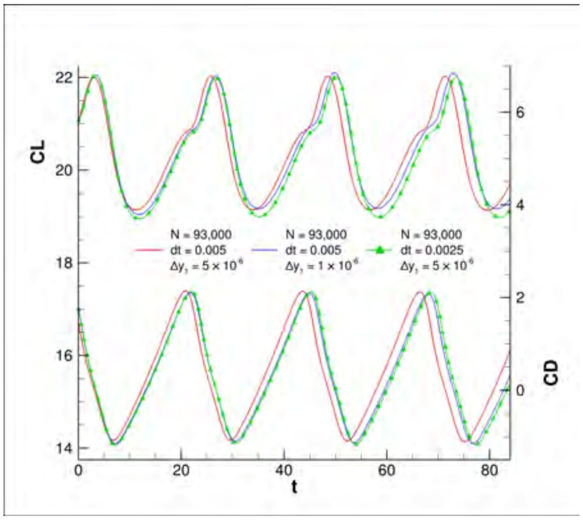

Figure 46: k-ω SST model validation cases.

The time-history coefficients of lift and drag results using the k-ω SST turbulence model are shown in Figure 46. Using this model, the CFJ cylinder measures a time-averaged $C_L = 20.36$. While this value is 11% lower than that of the flow field solution obtained from the S-A model, the difference is not large and the C_L still qualifies as a super-lift coefficient. Thus, since the k-ω SST turbulence model corroborates the super-lift coefficient and EAPG obtained by the S-A model, the results of the EAPG in this paper is believed to be within the uncertainty of the RANS models.

6 Conclusions

This paper presents the findings of a 2D numerical study of flows with EAPG enabled by Co-Flow Jet (CFJ) active flow control (AFC). The flow field is solved using a set of 2D Improved Delayed Detached Eddy Simulation (IDDES) equations with the one-equation Spalart-Allmaras turbulence model. A CFJ cylinder and CFJ airfoil with EAPG and attached flow are studied at Mach number 0.063 and Reynolds numbers $5.62 \times 10^5 - 1.68 \times 10^6$. With sufficiently high jet injection C_μ, the CFJ cylinder achieves lift coefficients up to $C_L = 26.72$, and the CFJ airfoil shows lift coefficients up to $C_L = 13.41$. The injection jet maintains subsonic flow for both cylinder and airfoil. Both cases maintain attached flow in a maximum adverse pressure gradients greater than their baselines up to 3 orders of magnitude. A spatial and temporal refinement study shows the solutions are mesh independent. The simulations using S-A model and SST mode only have the lift coefficient differed by 11% between CL= 22.89m and 20.365. It indicates that the EAPG phenomenon captured is within the uncertainty of the RANS models. All simulations showed sufficient convergence of the L2-norm and measured steady time-averaged results with characteristic time greater than at least 100.

The existence, magnitude, and causes of the extreme C_L and EAPG enabled by the CFJ merits further study. It is likely that the Spalart-Allmaras turbulence model [21] may not be suited to properly resolving flow attachment along the wall in the presence of such a significant adverse pressure gradient. Further studies with high fidelity simulation of LES, DNS, and experiment to verify the EAPG phenomenon are desirable.

7 Acknowledgments

The simulations are conducted on Pegasus super-computing system at the Center for Computational Sciences at the University of Miami.

Disclosure: The University of Miami and Dr. Gecheng Zha may receive royalties for future commercialization of the intellectual property used in this study. The University of Miami is also equity owner in CoFlow Jet, LLC, licensee of the intellectual property used in this study.

8 Tabular Data

Table 9: Time-Averaged Performance Metrics of CFJ Cylinder at Ma = 0.063, Re = 5.62×10^5

C_μ	C_L	C_D	P_C	P_{02}/P_{01}	C_L/C_D	C_L/C_{Dc}	C_L/P_c	$C_L - P_c$	Inj Ma	PG_s	PG_r
0.228	4.968	0.200	0.262	1.022	24.783	10.733	18.933	4.706	0.261	5.9	64.3
0.273	6.763	0.204	0.325	1.025	33.110	12.767	20.778	6.438	0.284	7.2	75.5
0.319	10.006	0.105	0.356	1.025	95.197	21.711	28.126	9.651	0.304	8.4	85.7
0.365	11.332	0.119	0.393	1.026	95.606	22.148	28.825	10.939	0.326	9.6	97.6
0.410	11.952	0.119	0.459	1.029	100.377	20.692	26.065	11.494	0.346	10.7	109.3
0.456	12.358	0.110	0.545	1.033	111.929	18.851	22.669	11.813	0.365	11.8	121.0
0.501	12.667	0.103	0.647	1.037	123.026	16.888	19.575	12.020	0.383	12.8	132.8
0.547	13.014	0.099	0.758	1.041	130.884	15.185	17.178	12.257	0.401	13.9	144.6
0.592	15.804	0.162	0.816	1.043	97.719	16.172	19.380	14.989	0.42	16.0	156.9
0.638	16.558	0.168	0.929	1.047	98.505	15.093	17.824	15.629	0.438	17.4	169.2
0.684	17.153	0.164	1.045	1.052	104.550	14.181	16.407	16.108	0.454	18.7	180.8
0.729	17.684	0.173	1.176	1.056	102.498	13.111	15.034	16.508	0.47	20.1	193.0
0.775	18.171	0.163	1.310	1.061	111.452	12.334	13.868	16.861	0.485	21.4	204.9
0.820	18.245	0.243	1.473	1.067	75.007	10.632	12.388	16.772	0.503	23.2	218.9
0.866	18.614	0.252	1.626	1.072	73.970	9.915	11.450	16.988	0.52	24.6	232.9
0.911	18.997	0.263	1.782	1.077	72.228	9.289	10.660	17.215	0.533	25.9	243.3
0.957	19.370	0.273	1.949	1.082	71.000	8.720	9.941	17.421	0.547	27.3	256.0
1.003	19.734	0.273	2.116	1.087	72.159	8.259	9.326	17.618	0.562	28.7	269.2
1.048	20.194	0.304	2.291	1.092	66.387	7.781	8.814	17.903	0.575	30.1	280.7
1.094	20.570	0.307	2.469	1.098	67.042	7.410	8.331	18.101	0.588	31.5	292.1
1.139	20.981	0.309	2.651	1.103	67.921	7.088	7.913	18.330	0.601	32.9	304.0
1.253	21.959	0.340	3.140	1.117	64.527	6.309	6.993	18.819	0.633	36.7	333.5
1.367	22.892	0.395	3.663	1.131	58.005	5.641	6.249	19.228	0.665	40.7	364.2
1.481	22.907	0.432	4.265	1.147	53.066	4.877	5.371	18.642	0.696	45.1	395.3
1.595	22.751	0.415	4.921	1.164	54.793	4.264	4.623	17.830	0.727	49.5	426.1
1.709	22.682	0.368	5.595	1.181	61.680	3.804	4.054	17.088	0.759	54.5	458.7
1.823	23.111	0.343	6.270	1.197	67.433	3.495	3.686	16.842	0.791	59.9	490.3
2.051	24.716	0.349	7.665	1.230	70.743	3.084	3.224	17.050	0.857	72.3	552.8
2.278	26.718	0.463	9.198	1.264	57.650	2.766	2.905	17.521	0.94	89.2	618.7

Table 10: Unsteady Performance of CFJ Cylinder at Ma = 0.063, Re = 5.62×10^5

C_μ	C_L	Stag. Point	History	CL_{max}	CL_{min}	CD_{max}	CD_{min}	St	Γ
0.228	4.968	Attached	Periodic	7.491	2.366	0.708	-0.485	0.048	3.855
0.273	6.763	Attached	Periodic	8.960	3.657	0.714	-0.747	0.041	4.554
0.319	10.006	Attached	Stable	10.006	10.006	0.105	0.105	0.000	5.031
0.365	11.332	Attached	Stable	11.332	11.332	0.119	0.119	0.000	5.699
0.410	11.952	Detached	Stable	11.952	11.952	0.119	0.119	0.000	6.033
0.456	12.358	Detached	Stable	12.358	12.358	0.110	0.110	0.000	6.234
0.501	12.667	Detached	Stable	12.667	12.667	0.103	0.103	0.000	6.360
0.547	13.014	Detached	Stable	13.014	13.014	0.099	0.099	0.000	6.519
0.592	15.804	Detached	Stable	15.804	15.804	0.162	0.162	0.000	7.779
0.638	16.558	Detached	Stable	16.558	16.558	0.168	0.168	0.000	8.127
0.684	17.153	Detached	Stable	17.153	17.153	0.164	0.164	0.000	8.410
0.729	17.684	Detached	Stable	17.684	17.684	0.173	0.173	0.000	8.669
0.775	18.171	Detached	Stable	18.171	18.171	0.163	0.163	0.000	8.872
0.820	18.245	Detached	Periodic	19.590	17.359	1.064	-0.581	0.037	10.671
0.866	18.614	Detached	Periodic	19.927	17.745	1.099	-0.591	0.039	10.541
0.911	18.997	Detached	Periodic	20.278	18.147	1.130	-0.595	0.041	10.926
0.957	19.370	Detached	Periodic	20.625	18.555	1.153	-0.596	0.043	11.180
1.003	19.734	Detached	Periodic	20.975	18.971	1.172	-0.587	0.043	10.989
1.048	20.194	Detached	Periodic	21.331	19.397	1.186	-0.570	0.049	11.380
1.094	20.570	Detached	Periodic	21.706	19.840	1.192	-0.558	0.048	11.595
1.139	20.981	Detached	Periodic	22.088	20.276	1.178	-0.558	0.049	11.861
1.253	21.959	Detached	Periodic	23.057	21.023	1.221	-0.548	0.051	12.521
1.367	22.892	Detached	Periodic	24.046	21.654	1.248	-0.570	0.050	13.211
1.481	22.907	Detached	Periodic	24.609	21.242	1.849	-1.224	0.040	13.946
1.595	22.751	Detached	Periodic	24.578	21.102	2.229	-1.605	0.038	13.946
1.709	22.682	Detached	Periodic	24.512	21.096	2.477	-1.696	0.039	13.749
1.823	23.111	Detached	Periodic	24.950	21.447	2.592	-1.619	0.041	13.619
2.051	24.716	Detached	Periodic	26.573	22.777	2.603	-1.019	0.048	13.752
2.278	26.718	Detached	Periodic	28.353	24.445	2.620	-1.423	0.052	14.195

Table 11: Time-Averaged Performance Metrics of CFJ Cylinder at Ma = 0.063, Re = 1.124×10^6

C_μ	C_L	C_D	P_C	P_{02}/P_{01}	C_L/C_D	C_L/C_{Dc}	C_L/P_c	$C_L - P_c$	Inj Ma	PG_s	PG_r
0.228	5.139	0.134	0.243	1.020	38.367	13.628	21.136	4.896	0.259	6.6	62.4
0.456	12.285	0.054	0.503	1.030	228.333	22.052	24.409	11.782	0.365	12.3	119.1
0.684	17.092	0.108	0.981	1.048	157.842	15.696	17.429	16.112	0.455	19.0	178.1
0.911	18.821	0.161	1.693	1.073	116.846	10.154	11.120	17.128	0.535	26.1	240.9
1.139	20.780	0.193	2.548	1.099	107.672	7.581	8.155	18.232	0.603	33.6	301.4
1.367	22.691	0.254	3.555	1.127	89.503	5.958	6.383	19.136	0.667	41.9	362.3
1.595	22.509	0.251	4.823	1.161	89.816	4.437	4.667	17.686	0.731	51.5	428.0
1.823	23.030	0.192	6.184	1.194	119.863	3.612	3.724	16.846	0.793	62.1	491.0
2.051	24.786	0.225	7.584	1.227	110.032	3.174	3.268	17.202	0.856	74.3	553.0

Table 12: Unsteady Performance of CFJ Cylinder at Ma = 0.063, Re = 1.124×10^6

C_μ	C_L	Stag. Point	History	CL_{max}	CL_{min}	CD_{max}	CD_{min}	St	Γ
0.228	5.139	Attached	Periodic	7.484	2.674	0.608	-0.533	0.045	3.839
0.456	12.285	Detached	Stable	12.285	12.285	0.054	0.054	0.000	6.226
0.684	17.092	Detached	Stable	17.092	17.092	0.108	0.108	0.000	8.439
0.911	18.821	Detached	Periodic	20.092	17.978	1.020	-0.690	0.041	10.892
1.139	20.780	Detached	Periodic	21.888	20.082	1.055	-0.674	0.050	11.767
1.367	22.691	Detached	Periodic	23.857	21.447	1.096	-0.721	0.050	13.068
1.595	22.509	Detached	Periodic	24.324	20.891	2.100	-1.773	0.038	13.636
1.823	23.030	Detached	Periodic	24.858	21.367	2.434	-1.729	0.041	13.788
2.051	24.786	Detached	Periodic	26.596	22.844	2.436	-1.086	0.048	14.069

Table 13: Time-Averaged Performance Metrics of CFJ Cylinder at Ma = 0.063, Re = 1.686×10^6

C_μ	C_L	C_D	P_C	P_{02}/P_{01}	C_L/C_D	C_L/C_{Dc}	C_L/P_c	$C_L - P_c$	Inj Ma	PG_s	PG_r
0.228	5.209	0.117	0.235	1.020	44.678	14.811	22.156	4.974	0.26	6.3	61.9
0.456	12.220	0.040	0.488	1.029	303.562	23.151	25.062	11.733	0.365	12.6	118.6
0.684	17.085	0.115	0.974	1.048	148.704	15.687	17.537	16.110	0.454	19.7	178.4
0.911	18.876	0.201	1.703	1.073	93.922	9.915	11.085	17.173	0.534	26.5	242.4
1.139	20.868	0.259	2.557	1.099	80.718	7.411	8.160	18.311	0.602	33.3	301.8
1.367	22.765	0.355	3.543	1.127	64.197	5.840	6.425	19.222	0.667	41.2	362.0
1.595	22.567	0.377	4.782	1.159	59.899	4.375	4.720	17.785	0.731	50.6	425.0
1.823	23.113	0.353	6.093	1.191	65.504	3.586	3.793	17.020	0.795	61.6	487.1
2.051	24.902	0.410	7.444	1.223	60.734	3.171	3.345	17.458	0.866	75.1	550.0

Table 14: Unsteady Performance Metrics of CFJ Cylinder at Ma = 0.063, Re = 1.686×10^6

C_μ	C_L	Stag. Point	History	CL_{max}	CL_{min}	CD_{max}	CD_{min}	St	Γ
0.228	5.209	Attached	Periodic	7.461	2.795	0.576	-0.547	0.044	3.829
0.456	12.220	Detached	Stable	12.220	12.220	0.040	0.040	0.000	6.225
0.684	17.085	Detached	Stable	17.085	17.085	0.115	0.115	0.000	8.452
0.911	18.876	Detached	Periodic	20.133	18.046	1.053	-0.647	0.042	10.865
1.139	20.868	Detached	Periodic	21.970	20.171	1.112	-0.605	0.050	11.898
1.367	22.765	Detached	Periodic	23.932	21.521	1.200	-0.620	0.051	13.083
1.595	22.567	Detached	Periodic	24.367	20.943	2.241	-1.659	0.038	13.890
1.823	23.113	Detached	Periodic	24.952	21.461	2.589	-1.582	0.041	14.038
2.051	24.902	Detached	Periodic	26.704	22.962	2.624	-0.897	0.049	14.047

Table 15: Performance Metrics of CFJ Airfoil at Ma = 0.063, Re = 5.62×10^5

C_μ	C_L	C_D	P_C	P_{02}/P_{01}	C_L/C_D	C_L/C_{Dc}	C_L/P_c	Inj Ma	Stag. Point
0.568	3.569	1.467	0.315	1.027	2.434	2.003	11.325	0.38	Attached
0.682	4.273	0.826	0.352	1.028	5.172	3.626	12.130	0.429	Attached
0.796	5.463	0.074	0.524	1.019	73.613	9.133	10.427	0.448	Attached
1.137	7.468	0.024	0.869	1.027	305.174	8.359	8.594	0.547	Attached
1.592	9.584	-0.019	1.552	1.041	-501.839	6.253	6.176	0.665	Attached
2.046	11.606	-0.051	2.593	1.062	-225.632	4.567	4.477	0.774	Attached
2.274	12.381	-0.070	3.303	1.076	-176.598	3.829	3.748	0.827	Detached
2.729	13.411	-0.097	5.004	1.106	-132.748	2.734	2.679	0.926	Detached

References

[1] P. Barrios, Y. Ren, and G.-C. Zha, “Simulation of 3d co-flow jet airfoil with integrated micro-compressor actuator at different cruise mach numbers.” AIAA Paper-2023-2118, AIAA SCITECH 2023 Forum, 23 Jan, 2023.

[2] G.-C. Zha, Y.-C. Yang, Y. Ren, and B. McBreen, “Super-lift and thrusting airfoil of coflow jet-actuated by micro-compressors.” AIAA Paper 2018-3061, AIAA AVIATION 2018, Atlanta, GA , 25 - 29 June 2018.

[3] Yang, Y.-C. and Zha, G.-C., “Super-Lift Coefficient of Active Flow Control Airfoil: What Is the Limit?.” AIAA Paper 2017-1693, AIAA SCITECH2017, 55th AIAA Aerospace Science Meeting, Grapevine, Texas, 9-13 January 2017.

[4] Y.-C. Yang and G.-C. Zha, “Simulation of airfoil stall flows using iddes with high order schemes.” AIAA Paper 2016-3185, AIAA AVIATION 2016, 46th AIAA Fluid Dynamics Conference, Washington, D.C., 13-17 June 2016 , 2016.

[5] J. Jeon, B. McBreen, Y. Ren, and G.-C. Zha, “Study of 3d flapped coflow jet wings for ultra-high cruise lift coefficient.” AIAA Paper-2023-4436, AIAA AVIATION 2023 Forum, 12 June, 2023.

[6] J. Jeon, Y. Ren, and G.-C. Zha, “Toward ultra-high cruise lift coefficient using flapped coflow jet airfoil.” AIAA Paper-2023-1008, AIAA SCITECH 2023 Forum, 23 Jan, 2023.

[7] Y. Wang and G.-C. Zha, “Study of Mach Number Effect for 2D Co-Flow Jet Airfoil at Cruise Conditions.” AIAA Paper 2019-3169, AIAA Aviation 2019, AIAA Applied Aerodynamics Conference, Dallas, Texas, 17-21 June 2019.

[8] Y. Wang and G.-C. Zha, “Study of Reynolds Number Effect for 2D Co-Flow Jet Airfoil at Cruise Conditions.” AIAA-2020-2666, AIAA Aviation Virtual Forum, 15-19 June, 2020.

[9] Y. Wang and G.-C. Zha, “Study of Mach Number Effect for 3D Co-Flow Jet Wings at Cruise Conditions.” AIAA Paper 2020-0045, AIAA SciTech Forum, 6-10 Jan, 2020.

[10] Y. Wang, Y.-C. Yang, and G.-C. Zha, “Study of Super-Lift Coefficient of Co-Flow Jet Airfoil and Its Power Consumption.” AIAA Paper 2019-3652, AIAA Aviation 2019, AIAA Applied Aerodynamics Conference, Dallas, Texas, 17-21 June 2019.

[11] Yang, Y.-C. and Fernandez, M. and Zha, G.-C., “Improved Delayed Detached Eddy Simulation of Super-Lift Flow of Co-Flow Jet Airfoil.” AIAA Paper 2018-0314, AIAA SciTech Forum, 2018 AIAA Aerospace Sciences Meeting, Kissimmee, FL, 8-12 January 2018.

[12] G.-C. Z. B. McBreen, K.-W. Xu, “Numerical study of extreme adverse pressure gradients enabled by co-flow jet.” AIAA Paper-2023-1430, AIAA SCITECH 2023 Forum, 23 Jan, 2023.

[13] Kewei Xu, Yan Ren, Gecheng Zha, “Numerical Analysis of Energy Expenditure for Co-Flow Wall Jet Separation Control.” AIAA Journal, doi.org/10.2514/1.J061015, 11 Jan 2022.

[14] K. Xu and G.-C. Zha, “Study of separation control using pulsed co-flow jet and its energy expenditure.” AIAA Paper-2023-0658, AIAA SCITECH 2023 Forum, 23 Jan, 2023.

[15] K.-W. Xu, Y. Ren, and G.-C. Zha, “Flow separation control by coflow wall jet.” AIAA Paper 2021-2946, AIAA Aviation 2021, 2-6 Aug. 2021.

[16] A. Smith, “High-Lift Aerodynamics,” *Journal of Aircraft*, vol. 12, pp. 501–530, 1975.

[17] T. O. G. Prandtl, Ludwig, *Applied Hydro- and Aeromechanics (Dover Books on Aeronautical Engineering)*. Dover Publications, 1934.

[18] V. E. Lockwood, “Lift generation on a circular cylinder by tangential blowing from surface slots.” NASA TN D-244, May 1960.

[19] P. Tokumaru and P. Dimotakis, “The lift of a cylinder executing rotary motions in a uniform flow,” *Journal of Fluid Mechanics*, vol. 255, pp. 1–10, 1993.

[20] Yang, Y.-C. and Zha, G.-C., “Super Lift Coefficient of Cylinder Using Co-Flow Jet Active Flow Control.” AIAA Paper 2018-0329, AIAA SciTech Forum, 2018 AIAA Aerospace Sciences Meeting, Kissimmee, FL, 8-12 January 2018.

[21] P. Spalart and S. Allmaras, “A One-equation Turbulence Model for Aerodynamic Flows.” AIAA-92-0439, 1992.

[22] R. C., “2dwmh: 2d nasa wall-mounted hump separated flow validation case..” Turbulence Modeling Resource, turbmodels.larc.nasa.gov, 2003.

[23] G. K. Schlichting H., *Boundary-Layer Theory.* ISBN-13 : 978-3540662709: Springer, 2001.

[24] A. Jameson, “Time dependent calculations using multigrid, with applications to unsteady flows past airfoils and wings.” Fluid Dynamics and Co-located Conferences. American Institute of Aeronautics and Astronautics, Oct. , 1991.

[25] Shen, Y.-Q. and Zha, G.-C. and Wang, B.-Y., “ Improvement of Stability and Accuracy of Implicit WENO Scheme,” *AIAA Journal*, vol. 47, No. 2, pp. 331–344, 2009.

[26] Shen, Y.-Q. and Zha, G.-C. and Chen, X.-Y., “ High Order Conservative Differencing for Viscous Terms and the Application to Vortex-Induced Vibration Flows,” *Journal of Computational Physics*, vol. 228(2), pp. 8283–8300, 2009.

[27] Shen, Y.-Q. and Zha, G.-C. , “ Improvement of the WENO Scheme Smoothness Estimator,” *International Journal for Numerical Methods in Fluids*, vol. 64, p. DOI:10.1002/fld.2186, 2010.

[28] Zha, G.C., Shen, Y.Q. and Wang, B.Y., “An improved low diffusion E-CUSP upwind scheme ,” *Journal of Computer and Fluids*, vol. 48, pp. 214–220, Sep. 2011.

[29] G.-C. Zha and E. Bilgen, “Numerical Solutions of Euler Equations by Using a New Flux Vector Splitting Scheme,” *International Journal for Numerical Methods in Fluids*, vol. 17, pp. 115–144, 1993.

[30] G.-C. Zha and E. Bilgen, “Numerical Study of Three-Dimensional Transonic Flows Using Unfactored Upwind-Relaxation Sweeping Algorithm,” *Journal of Computational Physics*, vol. 125, pp. 425–433, 1996.

[31] B.-Y. Wang and G.-C. Zha, “A General Sub-Domain Boundary Mapping Procedure For Structured Grid CFD Parallel Computation,” *AIAA Journal of Aerospace Computing, Information, and Communication*, vol. 5, No.11, pp. 2084–2091, 2008.

[32] Kewei Xu, Gecheng Zha, “System energy benefit using co-flow jet active separation control for a serpentine duct,” 2008.

[33] Lefebvre, A. and Dano, B. and Bartow, W. and Di Franzo, M. and Zha, G.-C., "Performance and Energy Expenditure of Co-Flow Jet Airfoil with Variation of Mach Number," *AIAA Journal of Aircraft*, vol. 53, pp. 1757–1767, 2016.

[34] Wang, B. Y and Zha, G.-C., " Detached-Eddy Simulation of a Co-Flow Jet Airfoil at High Angle of Attack ," *AIAA Journal of Aircraft*, vol. 48, pp. 1495–1502, 2011.

[35] Im, H.-S. and Zha, G.-C. and Dano, B. P. E., "Large Eddy Simulation of Coflow Jet Airfoil at High Angle of Attack," *Journal of Fluid Engineering*, vol. 136(2), p. 021101, 2014.

[36] K.-W. Xu and G.-C. Zha, "High control authority 3d aircraft control surfaces using co-flow jet," *AIAA Journal of Aircraft*, July 2020.

[37] Wang, B.-Y. and Haddoukessouni, B. and Levy, J. and Zha, G.-C., "Numerical Investigations of Injection Slot Size Effect on the Performance of Co-Flow Jet Airfoil ," *AIAA Journal of Aircraft*, vol. 45, pp. 2084–2091, 2008.

[38] Zha, G.-C. and Gao, W. and Paxton, C., "Jet Effects on Co-Flow Jet Airfoil Performance," *AIAA Journal, No. 6,*, vol. 45, pp. 1222–1231, 2007.

[39] Y.-Q. Shen and G.-C. Zha, "Large Eddy Simulation Using a New Set of Sixth Order Schemes for Compressible Viscous Terms ," *Journal of Computational Physics*, vol. 229, pp. 8296–8312, 2010.

[40] Zha, G.-C and Paxton, C. and Conley, A. and Wells, A. and Carroll, B., "Effect of Injection Slot Size on High Performance Co-Flow Jet Airfoil," *AIAA Journal of Aircraft*, vol. 43, 2006.

[41] B. P. E. Dano, D. Kirk, and G.-C. Zha, "Experimental Investigation of Jet Mixing Mechanism of Co- Flow Jet Airfoil." AIAA-2010-4421, (5th AIAA Flow Control Conference, Chicago, IL), 28 Jun - 1 Jul 2010.

[42] R. Piekert and F. Sadlo, "Topologically relevant stream surfaces for flow visualization." Conference: Proc. Spring Conference on Computer Graphics, April 2009.

[43] L. Perko, "Differential equations and dynamical systems, 3rd ed.." Springer-Verlag, New York. Inc. ISBN 0-387-95116-4, 2001.

[44] G. E. M., "Internal Flow: Concepts and Aplications." Cambridge University Press, 2004.

[45] Y. Wang and G.-C. Zha, "Study of Mach Number Effect for 2D Co-Flow Jet Airfoil at Cruise Conditions." AIAA Paper 2019-3169, AIAA Aviation 2019, AIAA Applied Aerodynamics Conference, Dallas, Texas, 17-21 June 2019.

[46] F. Menter, "Zonal Two Equation k-w Turbulence Models For Aerodynamic Flows," 06 July 1993 - 09 July 1993.

[47] P. Patel and G.-C. Zha, "Improved delayed detached eddy simulation of separated flow." AIAA-2020-3013, 2020 AIAA AVIATION Forum, June 15 - 19, 2020.

[48] Y. Liu, X. Guan, and C. Xu, "A production limiter study of SST-SAS turbulence model for bluff body flows," *Journal of Wind Engineering and Industrial Aerodynamics*, vol. 170, pp. 162–178, 2017.